KG^{2}B, a collaborative benchmarking exercise for estimating the permeability of the Grimsel granodiorite – Part 1: measurements, pressure dependence and pore-fluid effects

C. David, C Wassermann, Marc Fleury, Guillaume Berthe, Alexandra Amann-Hildenbrand, Bernhard Krooss, Joel Billiotte, Catherine Davy, Pierre Delage, Philipp Braun, et al.

KG²B, a collaborative benchmarking exercise for estimating the permeability of the Grimsel granodiorite: measurements, pressure dependence and pore-fluid effects

C. David[1], J. Wassermann[2], and the KG²B Team[3]*

[1]Université de Cergy-Pontoise, Laboratoire GEC, Cergy-Pontoise, France.

[2]Université de Cergy-Pontoise, Laboratoire L2MGC, Cergy-Pontoise, France.

[3]Complete list detailed in Appendix A.

Corresponding author: Christian David (christian.david@u-cergy.fr)

Key Points (140 characters max):

- A benchmarking exercise involving 24 laboratories was organized to measure the permeability of the Grimsel granodiorite
- The influence of pore fluid, sample size, pressure sensitivity and methods (steady-state, transient pulse, oscillation) are discussed
- The average permeability measured with gas is larger than that measured with liquid (mostly water) by a factor 2

Abstract

A benchmarking exercise involving 24 laboratories was organized for measuring the permeability of a single low permeability material, the Grimsel granodiorite, at a common effective confining pressure (5 MPa). In total 39 measurements were collected that allowed us to discuss the influence of (i) pore-fluid, (ii) measurement method, (iii) sample size and (iv) pressure sensitivity. Discarding some outliers from the bulk data set (4 out of 39) an average permeability of 1.11 10^{-18} m² with a standard deviation of 0.57 10^{-18} m² was obtained. The most striking result was the large difference in permeability for gas measurements compared to liquid measurements. Regardless of the method used, gas permeability was higher than liquid permeability by a factor ~2 (k_{gas}=1.28 10^{-18} m² compared to k_{liquid}=0.65 10^{-18} m²). Possible explanations are that (i) liquid permeability was underestimated due to fluid-rock interactions (ii) gas permeability was overestimated due to insufficient correction for gas slippage and/or (iii) gases and liquids do not probe exactly the same porous networks. The analysis of Knudsen numbers shows that the gas permeability measurements were performed in conditions for which the Klinkenberg correction is sufficient. Smaller samples had a larger scatter of permeability values, suggesting that their volume were below the REV. The pressure dependence of permeability was studied by some of the participating teams in the range 1 to 30 MPa and could be fitted to an exponential law $k=k_o.\exp(-\gamma P_{eff})$ with γ=0.093 MPa^{-1}. Good practice rules for measuring permeability in tight materials are also provided.

1. Introduction

Permeability is a property of a given porous medium which quantifies its ability to allow fluid flow. Since the introduction of Darcy's phenomenological law (Darcy, 1856), permeability characterization usually involves pressure gradient and flow measurements of a single fluid phase. In the field, such measurements may only provide apparent permeability estimates for rock masses including pore, crack and fracture networks which are usually saturated or partially saturated with several fluids (Zinszner & Pellerin, 2007). Estimates of the single phase (or intrinsic, or absolute) permeability (hereafter simply referred to as permeability) are typically made by laboratory testing of core samples, following a saturation or a drying procedure for, respectively, liquid or gas phase testing. In the case of liquids, fluid saturation can be assessed from the evolution of poroelastic parameters such as the isotropic Skempton coefficient (Makhnenko & Labuz, 2013) which is very sensitive to residual air, during a step by step back fluid pressure increase to dissolve trapped air bubbles (Wild et al., 2015a). For tight rocks, the sample preparation and saturation procedures can be particularly long and may disturb the original pore network. For example saturation can change the equilibrium between solid and fluid phases naturally present in clay rocks (Pearson et al., 2011; Wild et al., 2015b). The drying procedure can also have dramatic effects in the presence of clay minerals, causing desiccation cracks (Wild et al., 2015). Many observations have been made regarding perturbations and modifications of rock properties due to sampling processes and stress release effects during coring (Blümling et al., 2007; Schild et al., 2001).

Measuring the permeability of tight formations, which can potentially serve as seals for nuclear waste repositories and/or strata for geological sequestration of CO2, for instance, poses a

number of challenges. In addition to the traditional sources of errors that affect more permeable formations (e.g., sample selection, non-representative specimens, disturbance introduced during sample acquisition and preparation), rocks that are particularly tight and prone to solid-fluid interactions can be more sensitive to the methods, procedures and techniques used to acquire permeability data. In low permeability rocks, classical steady-state flow measurements may be very difficult to perform because of slow variations of the measured quantities (pore pressure, flow rate) and the long time needed for flow stabilization. Due to the long duration of flow experiments, variations in external conditions (typically ambient temperature) may occur, compromising the accuracy of permeability estimates. For this reason two other methods have been developed: the transient pore pressure (or pulse) method and the pore pressure oscillation method which is similar to a steady-state oscillatory method. The pulse decay method pioneered by Brace et al. (1968) involves applying a pressure step increase in an upstream reservoir and measuring the pressure variations with time in both upstream and downstream reservoirs connected to the sample. As pressure diffusion occurs through the rock sample, permeability can be estimated from decay of the differential pore pressure which follows a decreasing exponential law. Further knowledge on transient pulse tests was gained from parametric analysis of pore pressure diffusion processes in rocks by Hsieh et al. (1981) and Neuzil et al. (1981). The pulse method has been widely and successfully used both in crystalline and shaly rock samples during triaxial mechanical tests in the laboratory (Bourbie & Walls, 1982; Brace et al., 1968; Carles et al., 2007; Selvadurai et al., 2005). Other transient methods, like the drawdown method or the pressure build-up method (Martin, 1959) are particularly well adapted to use in the field in boreholes (Bossart et al., 2002; Jakubick & Franz, 1993; Wassermann et al., 2011). Transient methods can be applied step by step after re-equilibration periods during loading tests, providing discrete measurements of permeability. Continuous measurements have been developed in order to investigate loading effects on low permeability rocks and are more representative of the evolution of in situ conditions during reservoir activities. Such methods are based on continuous oscillatory flow and analysis of sinusoidal signals of pore pressure at both ends of a sample through phase lag and amplitude ratio (Fischer, 1992; Kranz et al., 1990; Song & Renner, 2007).

All the above methods assume Darcy flow and more or less steady state conditions during the measurements. The measured quantities in the pulse decay and steady-state flow experiments are more sensitive to ambient temperature variations than the phase shift or amplitude ratio continuously measured in the oscillatory method (Kranz et al., 1990). The pulse decay method has the advantage of being relatively easy to perform but requires appropriate selection of the reservoir volume compared to the pore volume of the tested sample (Hsieh et al., 1981). Derivative techniques have been developed to face such issues linked to the experimental apparatus (Lin, 1982; Trimmer et al., 1980). The oscillation technique also requires some experimental adjustments concerning mainly: i) the frequency of the forcing pore pressure signal — as pointed out by Song & Renner (2007), the frequency dependence of hydraulic properties could be a way to define scaling parameters of the pore structure and ii) the peak-amplitude of the forcing waveform which has to be small enough to avoid local poroelastic and fluid compressibility effects. Sometimes it is also a technical challenge to maintain a sinusoidal forcing signal. In addition to permeability, the oscillatory method allows estimation of other key parameters such as diffusivity and specific storage capacity (Song & Renner, 2007). Theoretically, permeability depends only on the pore structure of the material, and should be independent of the nature of the pore fluid used for the measurement (Muskat & Wyckoff, 1937). However, differences have been reported in the literature between water and gas permeability

measurements. Gas permeability estimations must take into account the gas compressibility, and the measured permeability is an apparent value that needs to be corrected for the so-called gas slippage effect: the "liquid equivalent" permeability can be obtained by applying the Klinkenberg correction (Klinkenberg, 1941) to gas permeability measurements made at different mean pore pressures. When the pore size is of the same order as the gas molecule mean free path, additional corrections have to be done to account for Knudsen diffusion (Anez et al., 2014; Ziarani & Aguilera, 2012). Whatever the fluid used, permeability measurements require also a sufficiently low flow rate to avoid inertial effects, otherwise the Forchheimer correction has to be applied (e.g. Rust & Cashman, 2004).

In order to bring a know-how about accurate transport property characterization in low permeability material, we proposed a benchmarking exercise involving 24 laboratories around the world using both direct (steady-state, transient, oscillatory) and indirect methods (pore and crack network imagery, modeling) to study fluid flow. Such an extensive benchmarking effort in rock physics has not been done before to our knowledge: the FEBEX benchmark study numerically modeled the results of a fluid injection test in the Grimsel Test Site (Alonso et al., 2005) and, within the framework of the SAFOD project, an inter-laboratory benchmark of physical rock properties measurements involving 20 research organizations was organized several years ago. In the SAFOD effort, measured rock properties were permeability, ultrasonic wave speed, electrical resistivity, friction and strength; however very few of the participating laboratories provided results, so that the outcome of this benchmark was never published (Lockner et al., 2009).

The selected material for the present benchmarking exercise came from a single meter scale rock volume in a well-known underground rock laboratory, the Grimsel Test Site (GTS) in Switzerland. The GTS consists of several meter long galleries of 3.5 meters diameter excavated at 450 m depth in 1983 in granite and granodiorite of the Central Aar massif in the Swiss Alps in order to perform in situ experiments in the context of nuclear waste storage research in Switzerland (Lieb, 1989). Here the objectives and organization of the benchmark will be presented, and then the permeability measurements data set will be analyzed and discussed.

2. The KG²B Project

Following a workshop on «The challenge of studying low permeability materials» that was held at Cergy-Pontoise University in December 2014, a benchmark in which several laboratories would estimate the permeability of a single material was proposed to the attendees. The material to be selected for this benchmark had to fulfill different criteria such as availability, homogeneity and scientific interest. Several options were examined until finally we selected the Grimsel granodiorite (Switzerland). The benchmark was named the "KG²B" project, which derived from "K for Grimsel Granodiorite Benchmark" where K stands for the symbol of permeability. Fresh cores from the Swiss Grimsel test site, an underground research laboratory in hard rock, were drilled during the coring campaign of a scientific project funded through the Swiss Competence Center of Energy Research – Supply of Electricity (SCCER-SoE), that was aimed at performing a series of demonstration experiments at various scales (up to 1 km) to support implementation of deep geothermal energy in Switzerland. From published work on the

Grimsel Granodiorite (Ota et al., 2003), we expected a porosity of about 0.7%, and permeability in the range of 0.1 to 1 10^{-18} m².

2.1. The Objectives and Organization of the Benchmarking Exercise

Multiple objectives were defined for the benchmark: (i) to compare the results for a given method, (ii) to compare the results between different methods, (iii) to analyze the accuracy of each method, (iv) to study the influence of experimental conditions (especially the nature of pore fluid), (v) to discuss the relevance of indirect methods and models, and finally (vi) to suggest good practice for low permeability measurements. Guidelines were given to the participants, in which they were requested to follow a number of mandatory instructions: (i) permeability should be measured along the same direction, (ii) permeability should be measured at 5 MPa effective pressure (a pressure high enough to prevent leakage, small enough to minimize crack closure), and (iii) rock samples should not experience any effective pressure higher than 5 MPa before the permeability measurement was done. Effective pressure was assumed to be the difference between confining and pore pressure: indeed experimental evidence was found to support this statement (see section on pressure dependence). No recommendations or requirements were made concerning the pore fluid, confining and pore pressures, sample size and method to be used for estimating permeability. However we requested that all of this information be reported on a results spreadsheet (David et al., 2017). The benchmark was designed as a "blind-test": other results were not shared with the participants until after they had submitted their own results. The participants were also encouraged, once the permeability at 5 MPa effective pressure was obtained, to study the pressure dependence of permeability, in particular by reproducing the in situ stress conditions (estimated effective pressure 30 MPa). Any additional data reported was also welcome, such as porosity values. This complementary data set is discussed in the companion paper.

2.2. The Participants

When the benchmark was announced, 30 laboratories from 8 different countries volunteered to participate. Three groups were forced to withdraw participation for different reasons (experimental setup not available, technical problems, work overload), one group was not able to provide the results in due time, and two others did not respond to our further solicitations. Ultimately, we received results from 24 laboratories that form the "KG²B Team". The complete list of participants who sent their results is given in alphabetic order in Appendix A. A dedicated website https:/labo.u-cergy.fr/~kggb/ was created, including in particular a web page where the progress of the project could be followed on the so-called "KG²B-wheel" (David et al., 2017) which was updated as soon as results were received from any of the participants. It took one year to collect all the results. Participants were regularly sent updates on the benchmark progress, to encourage those who had not yet sent their results.

2.3. The Selected Material

Two cores of Grimsel granodiorite, each about one meter long and 85 mm in diameter, were provided by our Swiss colleagues in September 2015. These cores were retrieved at a distance of 4 to 6 meters from the tunnel were the borehole has been drilled; the sampling region was expected to be sufficiently distant from the fracture network of the excavation damage zone

(EDZ) and the cores were therefore assumed to be free of tunnel induced damage. The cores were cut into small blocks at lengths requested by each participant (2 to 10 cm). Foliations are visible on the cores, at an angle of about 20-30° with respect to the core axis. The foliation is related to compositional banding of alternating dark biotite layers and quartz-rich layers (Schild et al., 2001). A thorough microstructural study is presented in the companion paper: the minerals identified are quartz, feldspars (albite, plagioclase), micas (muscovite, biotite) and apatite. Before blocks were sent to the participants, a quality check was performed on each block by the organizers at Cergy-Pontoise University. After drying the samples at 60°C for 24h, the P-wave velocity was measured at room conditions in three orthogonal directions. We observed that the P-wave velocity in the core axis direction increased with the distance from the tunnel, and decreased slightly with distance in the radial direction perpendicular to the foliation (David et al., 2017). This trend may result from mineralogical changes along the borehole or from the persistent influence of the excavation damage effects. A significant P-wave velocity anisotropy was found, due to the foliation inclination with respect to the core axis. It was necessary to require that all participants make permeability measurements in a common direction. This common direction was chosen for convenience as the core axis direction. Some laboratories performed additional permeability measurements in other directions, thus providing insight into the permeability anisotropy in the Grimsel granodiorite (see the discussion in the companion paper). The main result of this quality check was that reproducibility is acceptable.

3. Permeability Measurements at Constant Effective Stress

We will use the following convention for presenting the data set. Each lab was assigned a number in increasing order based upon the distance between their sample and the borehole mouth. Lab#01 worked on the sample closest to the borehole mouth (i.e. closest to the tunnel wall), and Lab#24 on the farthest sample (i.e. the deepest from the tunnel wall).

In the following analysis, the number of results is larger than the number of laboratories in the KG²B team for several reasons: (i) some laboratories tested several small samples sub-cored from the original core, (ii) some laboratories made different kinds of measurements on a single sample. Before permeability measurements were made, the samples were systematically dried before being saturated with the working fluid. Our benchmarking exercise specifically excludes two-phase flow and relative permeability estimation which, although important, imply higher order of complexity.

3.1. General Characteristics of the Data Set

In Table B1 of Appendix B we report the location of each sample (distance from the tunnel), the size of the sub-cored samples on which permeability was measured, the method applied and the fluid used to conduct the measurements. In total we collected 45 permeability values from measurements (39) and modeling (6). Most of the results (56%) come from direct measurements using gas as the pore fluid (Figure 1a), about 31% of the results come from direct measurements using liquids (mostly water) as the pore fluid, and only six results (about 13%)

were collected from models using microstructural data to predict the permeability. Here we will only consider the experimental data set, while the modeling data set will be presented in the companion paper. Figure 1b summarizes the techniques which were used.

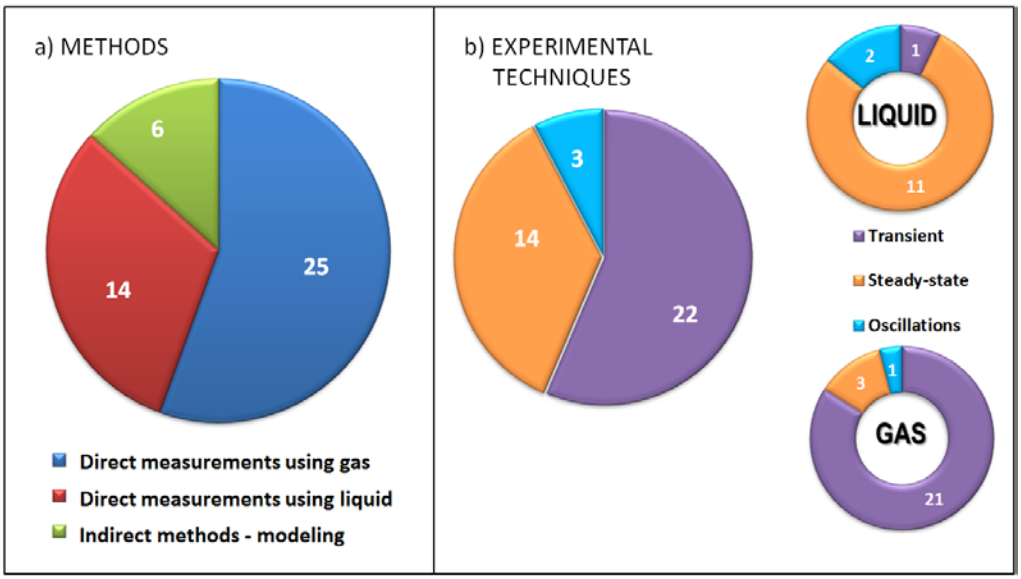

Figure 1. a) Methods used in the benchmark and b) techniques used for the experiments, global distribution (left) and distribution by working fluid type (right).

Regardless of the nature of the pore fluid, the transient technique was the most used (56%) followed by the standard steady-state method (36%), a direct application of Darcy's law. A few laboratories used the pore pressure oscillation technique (8%). The distribution is, however, very different if one takes into account the fluid used to measure the permeability. In experiments with liquid as the working fluid, 78% of the results were obtained with the steady-state technique. In contrast, with gas as the working fluid, only 12% of the results were obtained with the steady-state technique and 84% of the results come from the pulse transient technique. Various gases were used: mostly nitrogen, but also argon, helium and air.

3.2. Statistical Analysis of the Raw Data Set

The complete data set is reported in Table B2 of Appendix B. Here we present the statistical analysis for all measured permeability values at 5 MPa effective pressure in the core axis direction only (no anisotropy effect included), regardless of the method, pore fluid or sample size (Figure 2). For the complete data set, permeability ranges between 0.05 and 8.35 10^{-18} m², with an average value of 1.47 10^{-18} m² and a high standard deviation of 1.55 10^{-18} m². We identified four outliers (three in the last bin, one in the first bin in Figure 2) with permeability higher or lower by a factor three than the average permeability. It is, consequently, preferable to use the median (1.18 10^{-18} m²) and interquartile range (1.07 10^{-18} m²) as estimators of the permeability statistics. If we remove the four outliers, we find a range of permeability spanning one order of magnitude (between 0.20 and 2.6 10^{-18} m²) with a mean value of 1.11 10^{-18} m² close to the median (1.12 10^{-18} m²), and a standard deviation significantly reduced (0.57 10^{-18} m²). These values are in good agreement with the Grimsel granodiorite values reported by (Schild et al., 2001).

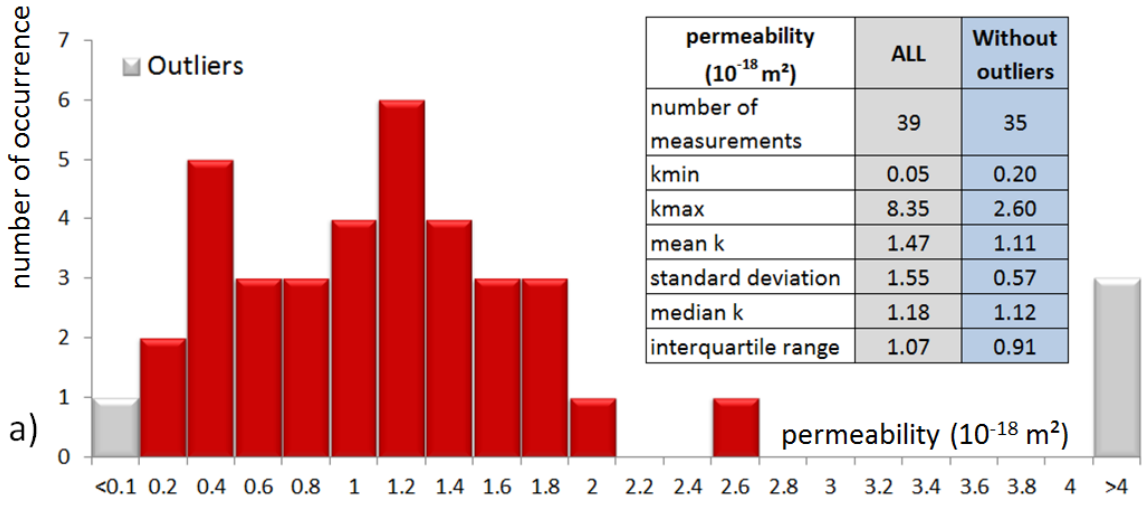

permeability (10^{-18} m²)	ALL	Without outliers
number of measurements	39	35
kmin	0.05	0.20
kmax	8.35	2.60
mean k	1.47	1.11
standard deviation	1.55	0.57
median k	1.18	1.12
interquartile range	1.07	0.91

Figure 2. Statistical distribution of the raw data set for all methods, fluids and sample size. Each label gives the central value of each bin (e.g. bin 0.2 corresponds to the range [0.1, 0.3]).

3.3. Influence of the Pore Fluid

Considering only the measurements in the core axis direction ("axial" flow), the 39 permeability values at 5 MPa effective pressure (Figure 2) can be divided into two sub-sets based on the nature of the pore fluid (gas or liquid) used to measure the permeability. The statistical distribution of these two subsets exhibits two overlapped distributions (Figure 3) and defines possible new outliers for the gas group: 2.6 10^{-18} m² (extrapolated value and poorly defined stresses) and 0.2 10^{-18} m². The influence of these possible gas outliers is low.

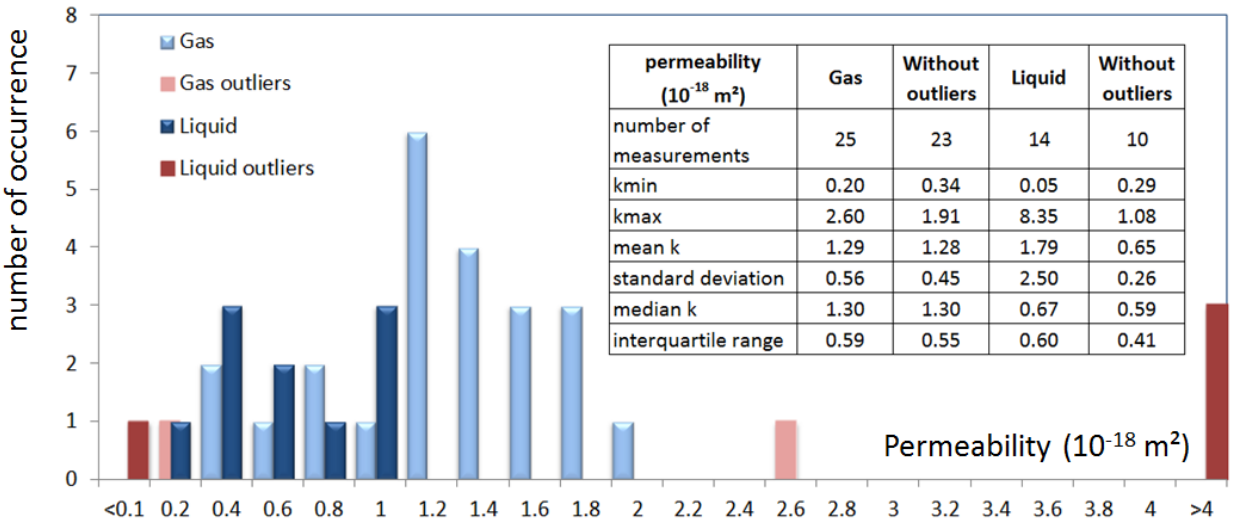

permeability (10^{-18} m²)	Gas	Without outliers	Liquid	Without outliers
number of measurements	25	23	14	10
kmin	0.20	0.34	0.05	0.29
kmax	2.60	1.91	8.35	1.08
mean k	1.29	1.28	1.79	0.65
standard deviation	0.56	0.45	2.50	0.26
median k	1.30	1.30	0.67	0.59
interquartile range	0.59	0.55	0.60	0.41

Figure 3. Statistical distribution of measured permeability values as a function of the working fluid.

A first analysis shows that the statistical parameters of the gas sub-set are about twice those of the liquid sub-set without outliers. Whereas the lowest outlier value seems to reflect to a

bad measurement, the higher ones probably owe to anomalous samples.

Permeability measurements using gas and liquid on a single sample were carried out by two labs with the following results: 1.3 & 0.94 10^{-18} m² @5MPa (Lab#09) and 34 & 28 nD @27MPa (Lab#23) respectively, giving a 1.3 ratio between gas and liquid permeability values. In both cases, the gas pressure was higher than 1.7 MPa and the Klinkenberg correction should be small. However successive permeability measurements on a single sample induce a complex history of loading and unloading that could generate irreversible changes in the porous space and therefore variations in measured permeability values.

Each team described the protocol used to saturate the porous space of the tested samples. There is no basis for associating low permeability values with incomplete saturation or to low pore pressures. Each lab which used a low gas pressure, attempted accurate evaluation of the Klinkenberg slip factor *b*.

Some labs provided several values of permeability by using the same sample with different gases, pore pressures and confinement pressures at constant effective pressure. Some labs used several sub samples from their initial piece of core. To remove the large weight of repetitive measurements, a single value for each lab was obtained by replacing multiple values by their average. The reduced data set contains 20 permeability values. Removing two outliers in the gas subset (light blue diamonds), the set of data was further reduced to 18 values: 11 for the gas subset and 7 for the liquid subset (Figure 4).

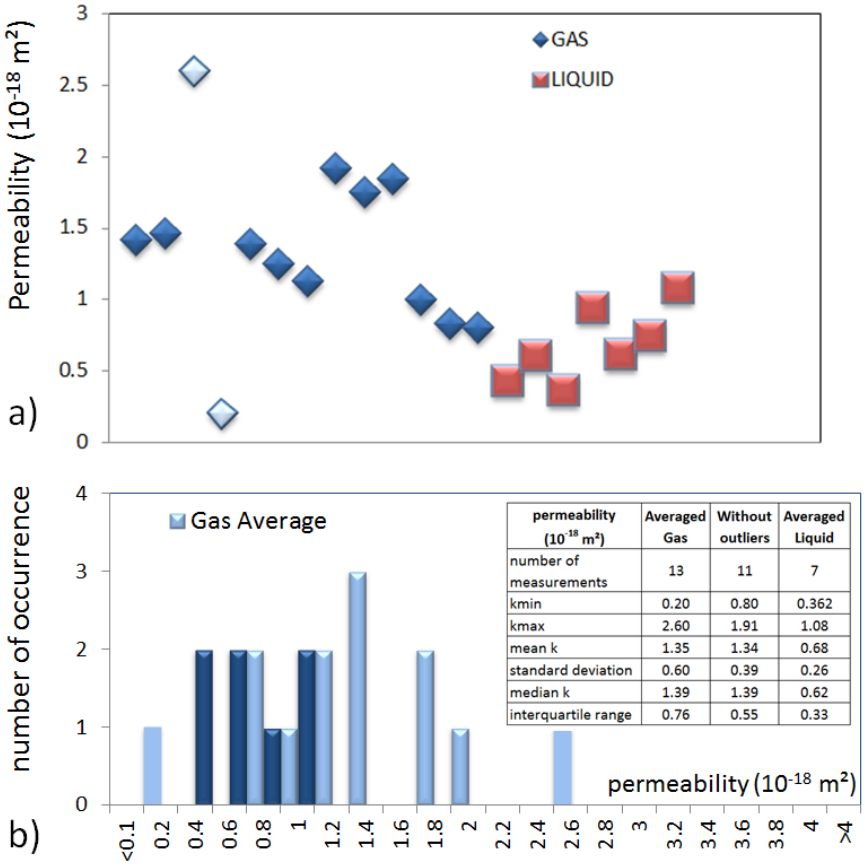

permeability (10^{-18} m²)	Averaged Gas	Without outliers	Averaged Liquid
number of measurements	13	11	7
kmin	0.20	0.80	0.362
kmax	2.60	1.91	1.08
mean k	1.35	1.34	0.68
standard deviation	0.60	0.39	0.26
median k	1.39	1.39	0.62
interquartile range	0.76	0.55	0.33

Figure 4. a) Average permeability values at a 5MPa effective pressure for each lab (data are ordered by lab number) and b) statistical parameters for these average values.

The overlapping of gas and liquid sub-sets is now reduced and this new representation of the data clearly confirms that measured gas permeability values tend to be larger than liquid permeability values by a factor of about two. This significant difference leads us to separate both subsets in the following discussion.

3.4. Influence of the Distance to the Tunnel

The permeability as a function of distance to the tunnel (Figure 5) shows no clear trend. David et al. (2017) reported P-wave velocity measurements at room temperature and unconfined conditions on the original core samples: they observed that P-wave velocity in the core axis direction increases with distance from the tunnel. The P-wave velocity increases linearly from ~4200 m/s at a distance of 4.2 m to ~4600 m/s at 5.7 m, and then jumps to a value close to 4800 m/s from 5.7 to 6 m. Between 4.2 and 5.7 m, the average gas permeability seems to be relatively constant, whereas the average liquid permeability seems to increase slightly. The observed trend in P-wave velocity may result from changes in mineralogy or foliation orientation along the borehole. This trend could also be linked to a varying Borehole Damage Zone which induced different stress release patterns from the tunnel to the deepest part of the borehole. Between 5.7 m and 6 m, the average gas permeability seems to decrease, which could be correlated with the observed 200 m/s jump in P wave velocity. Both observations could reflect a preexisting crack density (Fortin et al., 2011), which is lower for the samples located between 5.7 and 6 m.

However, only 3 samples are located in this interval, so that we cannot draw any firm conclusion on the effect of sample location (distance to tunnel) or porosity (see companion paper).

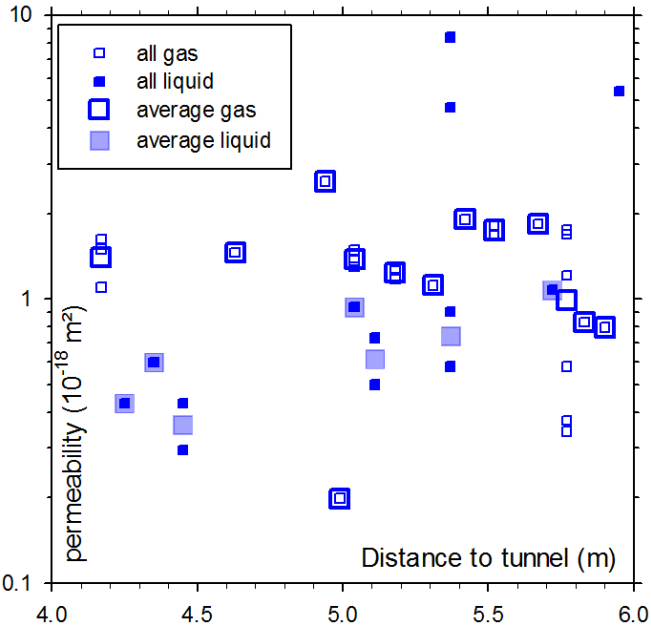

Figure 5. Measured axial permeability vs. distance to the tunnel from which the long cores were drilled.

3.5. Influence of the Sample Size

No recommendations were made with respect to sample size for permeability estimation. Most of the laboratories chose to sub-core the provided material (Table B1) and prepared small samples (volume ~20 cm^3, length 2-5 cm) in order to reduce the time required for completing the permeability measurements (David et al., 2017). Two laboratories decided to work directly on the original cores without sub-coring, whereas one group used a special device designed to work on tiny samples or chips (Lenormand et al., 2010). Permeability measurements with gas (open symbols) or liquid (solid symbols) are plotted in Figure 6a as a function of sample length in the direction of flow. As mentioned previously there is a wide range of permeability values (about two orders of magnitude), and the scatter appears larger for smaller samples, while little variation is found for the longest ones. This size dependence can be linked to the magnitude of the Representative Elementary Volume (REV), which may be large in the case of the Grimsel granodiorite because the grain size can be up to 2 cm (Schild et al., 2001). In Figure 6b a density map obtained from micro-CT scanning reveals the size of mineralogical heterogeneities. Although the density map is not necessarily correlated with pore network heterogeneity, one may expect an REV size larger than a few centimeters.

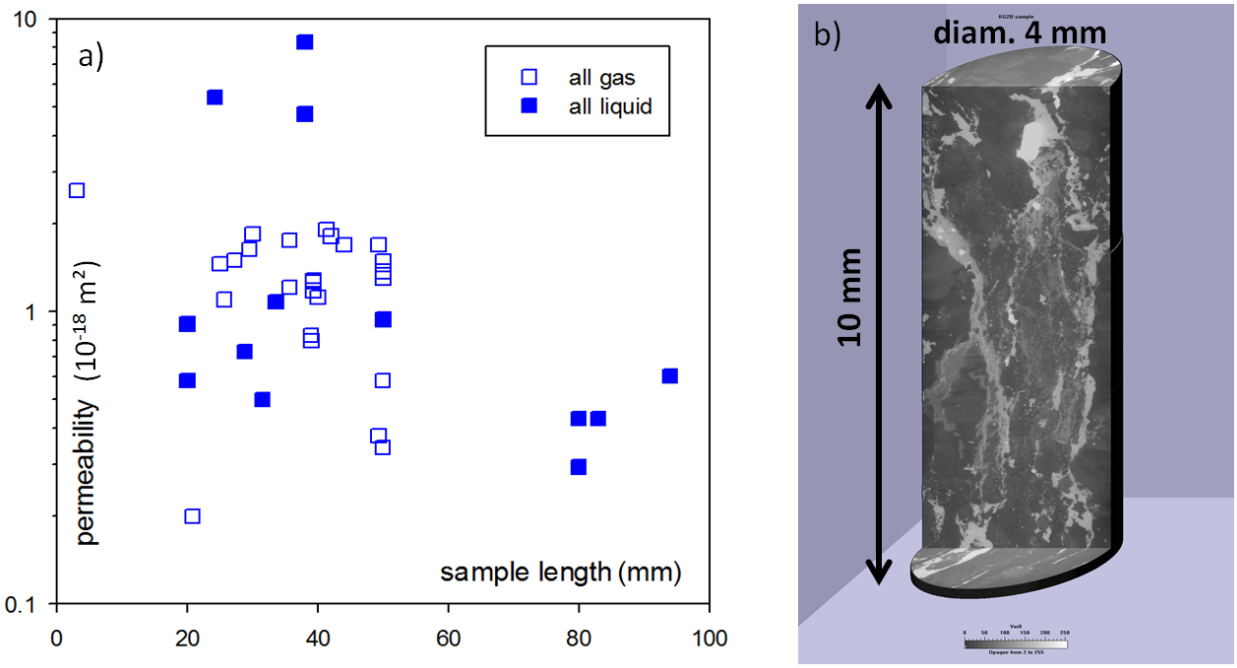

Figure 6. a) Measured axial permeability values vs. sample length in the flow direction. b) 3D reconstruction from micro-CT images obtained on a small volume of Grimsel granodiorite (voxel size 5 µm).

The sample length L has also a significant influence on the time required to establish steady-state flow conditions. Assuming no Klinkenberg effect, the duration of the transient scales as $(\mu C_f \phi/k)L^2$ with ϕ the porosity, k the permeability, C_f the fluid compressibility and μ the fluid viscosity. In addition there is a non-linear effect of mean pore pressure that can be quantified using numerical simulation. Taking k=1.0 10^{-18} m² and ϕ=1% for the Grimsel granodiorite, the transient time at low fluid pressure (< 1 MPa) is about 15 seconds for a one centimeter long sample, but increases to about 30 minutes for a ten centimeter long sample. At higher fluid pressure (~10 MPa) the transient time is shorter, about 2 minutes for a ten centimeter long sample. As stability is generally obtained after a few minutes, due to the relatively high permeability and low porosity, the transient is not likely to be a source of error for the KG²B measurements. However for a sample in the nanodarcies range (10^{-21} m²), the stabilization time for a similar measurement at low pressure on a 10 cm plug would be multiplied by 1000 (20 days!).

3.6. Influence of the Experimental Method

Steady-state measurements with gas were systematically corrected for the Klinkenberg effect. Not all transient measurements with gas were corrected for the Klinkenberg effect when the pore pressure was higher than 3 MPa. Several transient techniques were used to extract permeability from the recorded pressure decay data, including the standard transient pulse approximation (Brace et al., 1968), a complex transient inversion scheme that additionally provides specific storage (based on (Kranz et al., 1990)) and the more recent step decay method that provides the intrinsic permeability, porosity and Klinkenberg coefficient for gas

measurements in tight rocks (Lasseux et al., 2012). In Figure 7 the data set is divided into three groups according to the method used for measurements (SST for steady-state, PLS for transient pulse, and OSC for pore pressure oscillation). For each sub-group we also separate gas (open symbols) and liquid (solid symbols) measurements. For each subgroup, we estimated an average permeability value, omitting outliers. The average value for the transient pulse method (1.27 10^{-18} m²) is the highest, and that for the steady state method is the smallest (0.78 10^{-18} m²). For the pore pressure oscillation method, there are only three values available, so it is difficult to draw any statistically meaningful conclusion. Notice however that there is a great overlap between the division in terms of testing and the division in terms of working fluid (SST mostly liquids and PLS mostly gases).

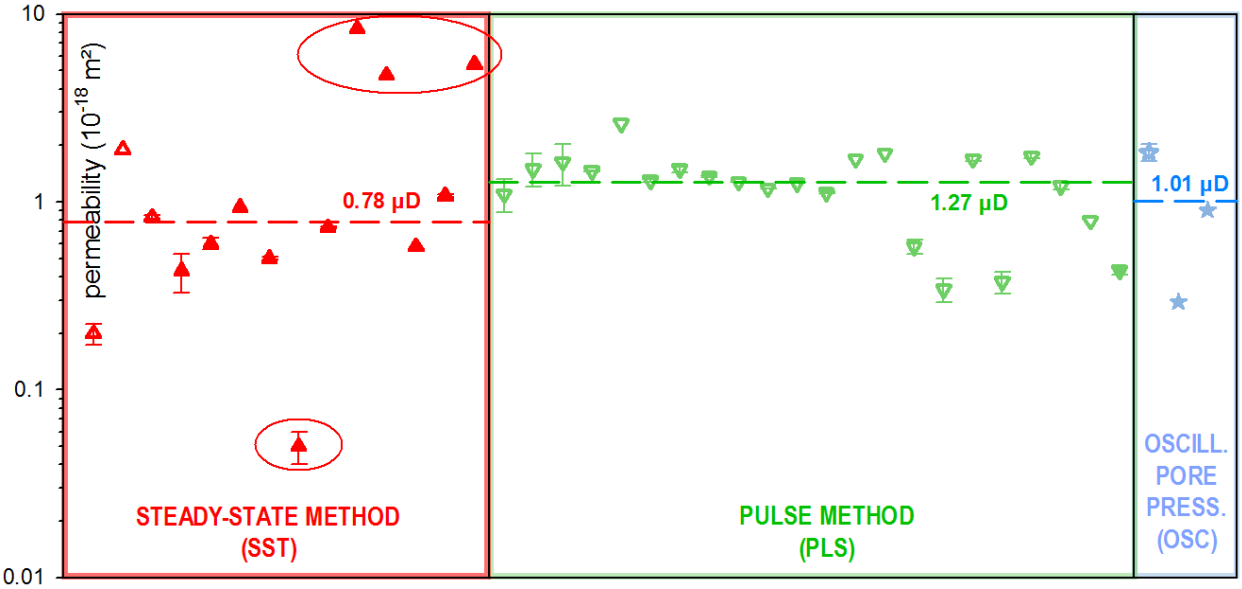

Figure 7. Measured axial permeability for the different techniques used with error bars when known (data points are ordered by lab number in each group). Open symbols correspond to measurements using gas. Dashed lines correspond to the average permeability value per method (without the outliers highlighted by ellipses).

To address this problem, we analyzed results provided by four teams who measured permeability on the same sample using different methods but the same pore fluid, sometimes at different pressure conditions (Lab#18). Figure 8 is a cross-plot of permeability using one particular method vs. permeability using another one. For this limited set of measurements, the permeability values are such that $k_{SST} < k_{OSC} < k_{PLS}$ which is the same order derived from statistical analysis on the three subgroups (Figure 7).

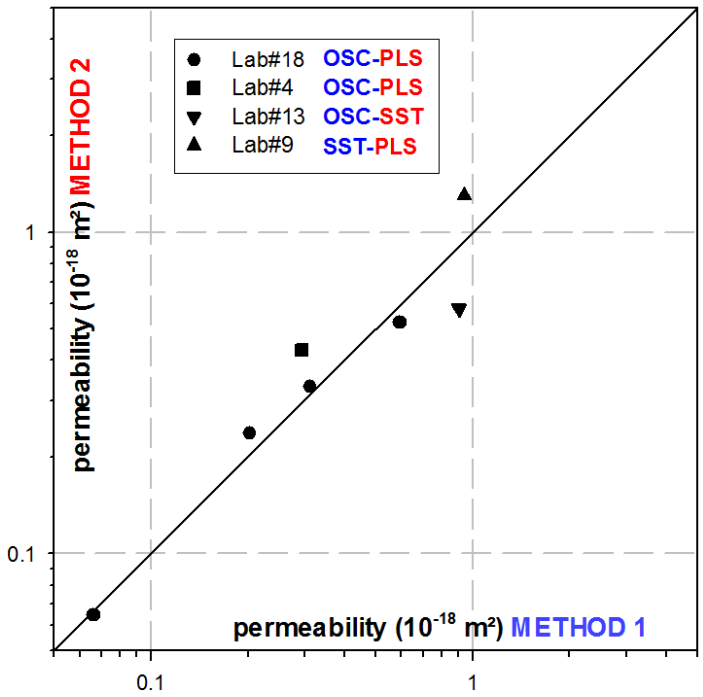

Figure 8. Comparison of permeability values for the same sample under the same pressure condition but using two different techniques. OSC = oscillating pore pressure method; SST = steady-state flow method; PLS = transient pulse method.

3.6.1. Example of Steady-state Flow Method for Permeability Determination

[Contribution of Lab#19] Permeability was measured on a section of whole core using the steady-state flow technique at a series of effective pressures and pore pressure gradients. Normally, sub-cores would be prepared from the original samples for testing. However, since the starting material had relatively large grain size, we decided that the best determination of average permeability would be obtained if the entire sample were tested. In this case, the core circumference, which was smooth and even, was used without modification and faces were ground flat and parallel using a diamond wheel on a surface grinder. The resulting sample, shown in Figure 9a, had physical dimensions of diameter = 8.3348 ± 0.0008 cm and height = 3.3617 ± 0.0005 cm.

Stainless steel end caps with 1.5 mm-diameter center holes and groove patterns on faces were placed on either end of the sample. Fine mesh stainless steel screen was placed between end caps and the sample to provide uniform pore pressure on sample faces. Shrink tubing covered the sample + end cap assembly which was then cast in 2-part polyurethane (approximately 5 mm thickness) to isolate the sample from the silicone oil confining fluid (Figure 9b). A coiled stainless return tubing provided pore fluid access to the bottom end cap.

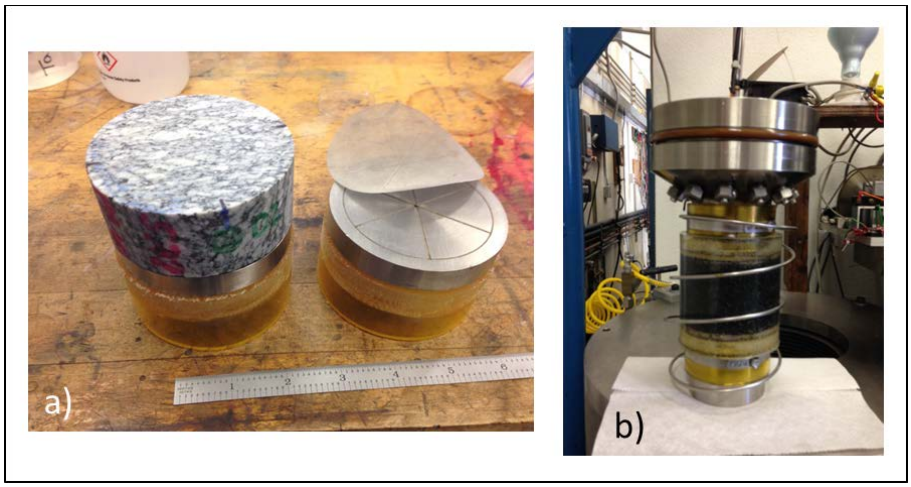

Figure 9. a) Whole core KG²B test sample with stainless steel end caps and stainless screen that assures uniform pore water access to sample faces. b) Sample assembly, including coiled return pore fluid line, is jacketed and ready to place in the pressure vessel.

This assembly was placed in a pressure vessel and an initial confining pressure, P_c, of 2 MPa was applied. The pore pressure system was evacuated and then pressurized to P_p = 1 MPa with deionized water. P_c and P_p were then increased together to assure that effective pressure ($P_{eff} = P_c - P_p$) never exceeded 2 MPa. The low-aspect-ratio cracks that provide flow paths in this crystalline rock are sensitive to effective pressure and have memory of past pressure history. Therefore, it is important that the target test pressure is not exceeded during sample pressurization.

Evacuation of the combined sample + pore pressure system, prior to saturation, is important in a low porosity sample to prevent air bubbles that would alter the fluid flow paths being trapped in the pore space. Conducting permeability tests at elevated pore pressure further reduces the risk of spurious measurements by compressing and dissolving remnant air bubbles that might remain trapped in pore space. The sample assembly in the pressure vessel, as well as the pore pressure pump and flow rate sensor were enclosed in a temperature-controlled chamber that maintained 23.5 ± 0.1°C. For steady flow tests in low permeability samples, variations in ambient temperature can become the primary source of uncertainty in determining permeability, since room temperature changes produce fluid volume fluctuations that appear as transients in flow rate (Morrow et al., 2014, Figure A1)

Confining pressure, up-stream (P_{UP}) and down-stream (P_{DOWN}) pore pressure were independently computer controlled. Reported effective pressure is defined as $P_{eff} = P_c - P_p = P_c - (P_{UP} + P_{DOWN})/2$. Pressure drop across the sample is just $\Delta P = P_{UP} - P_{DOWN}$. The pore pressure generator on the up-stream side of the sample recorded the change in pore volume (V_P) needed to maintain constant pressure with a precision of 10^{-5} cm^3. This volume change was used to determine flow rate, $Q = dV_P/dt$. Once the pressure drop across the sample is established and a steady state flow condition is attained, permeability k can be calculated from Darcy's law

$$k = \left(\frac{\mu L}{A}\right) Q/\Delta P \qquad (1)$$

where μ is dynamic viscosity and L and A are the length and cross-sectional area of the sample. Dynamic viscosity of water at 23.5°C is 0.921 10^{-3} Pa.s and L/A for this sample is 0.06161 cm^{-1}. As an example, a flow measurement at P_c = 30 MPa, P_{eff} = 5 MPa and ΔP = 0.946 MPa resulted in k = 1.068 x 10^{-18} m^2.

This reported permeability is of limited use without estimating errors. We next consider different methods for determining confidence intervals for the permeability measurements. The first method is to take multiple measurements of k and compute a mean value and standard error. We performed a series of 10 flow tests at P_{eff} = 5.0 MPa and at varying pore pressure gradients that produced both forward and reverse flow (Figure 10). If we assume that the individual determinations of k are random samples from the same distribution, and the 'true' permeability is represented by the mean of the distribution, then uncertainty can be expressed as standard error of the measurements. In this case, permeability, based on ten measurements, is k = (1.04 ± 0.01) x 10^{-18} m^2.

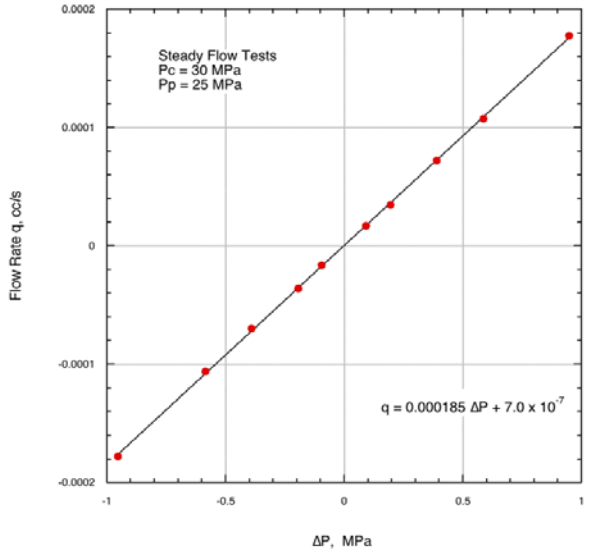

Figure 10. Permeability tests at P_{eff} = 5.0 MPa. Flow rate is a linear function of pressure gradient, ΔP, and using equation (1) gives k = (1.04 ± 0.01) x 10^{-18} m^2.

An equivalent method is to compute a least squares fit to the data in Figure 10 to provide the ratio $Q/\Delta P$. The result, including a calculation of the formal error is $\partial q/\partial \Delta P$ = 0.00185 ± 0.00001 cc/MPa, and applying equation (1) leads to a similar estimate of permeability.

A more complete measure of uncertainty includes consideration of errors in all of the variables on the right-hand side of equation (1). In this case, an uncertainty of ±0.1°C for the environmental chamber implies an uncertainty of ±0.002 10^{-3} Pa.s in viscosity (*i.e.*, ±0.2%). Uncertainties in physical sample dimensions (L/A) are estimated to be only ±0.03% and errors in ΔP are 0.001 MPa. Taken together, these contribute uncertainty of approximately ±0.5% in computing k. The final quantity to consider is the flow rate Q. The displacement transducer that measures V_P has a linearity of about 0.05% which limits the accuracy of determining Q. During a permeability test, V_P is sampled ten times per second and averaged at 1 s intervals. If we assume that the errors in measuring V_P are uncorrelated, we can divide the total measurement time into N intervals of equal length and estimate a Q_i for each interval. Then, the mean of the Q_i's provides an estimate of Q and the standard error provides an estimate of the uncertainty in Q. Using this

approach, with the standard recording interval used in this study of approximately 2500 s, accuracy in determining q was typically ±0.5%. Taken together with the uncertainties in the other variables, we estimate a total uncertainty in determining k of approximately 1%. This is in close agreement with the confidence interval quoted above and probably represents the best accuracy that we can expect to achieve with the current test system. Notice that the two largest contributions to uncertainties in determining permeability are variations in ambient temperature and uncertainties in determining Q. Some improvement in accuracy can be gained by sampling flow rate over longer intervals. However, accuracy in Q will improve, at best, as $(\text{time})^{1/2}$ and fluctuations in ambient temperature will ultimately limit accuracy. The importance of controlling ambient temperature cannot be overstated. The viscosity of water decreases by about $0.02\ 10^{-3}$ Pa.s/°C, so an error of 1°C in measurement temperature will result in a 2% error in calculated permeability.

3.6.2. Example of Transient Method for Permeability Determination

[Contributions of Lab#11 and Lab#12] The transient (or pulse) method (Bruce et al., 1953) consists of instantaneously applying a pulse of differential pore fluid pressure across the sample that will re-equilibrate with time by fluid flow through the sample. An interpretative model was reported later by (Brace et al., 1968). The permeability is derived from the time-dependent decrease of the upstream pore fluid pressure $P_{UP}(t)$, which can be approximated by an exponential law:

$$P_{UP}(t) - P_{\infty} \propto e^{-\alpha t} \text{ with } \alpha = \frac{kA}{\mu C_f L}\left(\frac{1}{V_{UP}} + \frac{1}{V_{DOWN}}\right) \quad (2)$$

where P_{∞} is the final upstream pressure, k the permeability, L and A the sample length and cross-section area respectively, μ the fluid viscosity, C_f the fluid compressibility and V_{UP} and V_{DOWN} the volume of the tanks connected to the upstream and downstream end of the sample respectively. The permeability of a Grimsel granodiorite sub-core (length = 40.10 mm; diameter = 19.74 mm) was measured in a high pressure vessel (maximum confining pressure 50 MPa) at room temperature using water as the confining medium and argon as pore fluid (Figure 11a). Prior to experiments, the sample was vacuum dried at 40°C for 48 hours, a period beyond which no additional mass decrease was recorded. To apply the confining pressure to the sample and avoid any leak, the sample was inserted in a rubber sleeve clamped onto end-pieces.

The decay through time of the upstream gas pressure P_{UP} is monitored whereas the downstream gas pressure P_{DOWN} is kept constant at atmospheric pressure P_{ATM}, that is $P_{\infty} = P_{DOWN} = P_{ATM}$ and the term $1/V_{DOWN}$ of equation (2) can be neglected. This configuration was shown to be the optimal one for a pulse-decay experiment (Jannot et al., 2007). Since the experiments are run at constant temperature (T = 20°C) and low gas pressure (≤ 0.5 MPa), one may also assume that the gas compressibility C_f can be approximated by $C_f = 1/P_{MEAN}$, where $P_{MEAN} = (P_{UP} + P_{DOWN})/2$ is the mean gas pressure in the sample. Then, by calculating the time derivative of equation (2), one obtains the following equation relating the gas permeability k_{gas} to the evolution of the upstream gas pressure:

$$k_{\text{gas}} = \frac{\mu_{\text{Ar}} L}{A} \frac{V_{\text{UP}}}{P_{\text{MEAN}} \Delta P} \left| \frac{dP_{\text{UP}}}{dt} \right| \quad (3)$$

where μ_{Ar} is the viscosity of Argon (= 2.21 10^{-5} Pa.s at 20°C) and $\Delta P = P_{UP} - P_{DOWN}$ is the gas pressure difference across the sample. Due to the narrow flow path in such a low permeability rock, the Klinkenberg correction must be carried out (see the section devoted to slip flow). Three confining pressure levels were tested: 1, 2 and 5 MPa. For each pressure level, the sample was allowed to rest in the cell for one night. The upstream inlet gas pressure is then increased to 0.5 MPa, the outlet downstream gas pressure is maintained constant at atmospheric pressure and the outlet gas volume flow rate Q^{V}_{DOWN} is measured. Once the latter has stabilized, the inlet valve is closed and the upstream gas pressure is allowed to decrease. In Figure 11b, we show the pressure decay curves obtained at the various confining pressure levels. Note that in contrast to experiments using liquids (with constant compressibility), the pressure decay is not linear on the semi-log plot as expected from equation (2): this is so because the gas compressibility depends on the mean pressure which decreases with time.

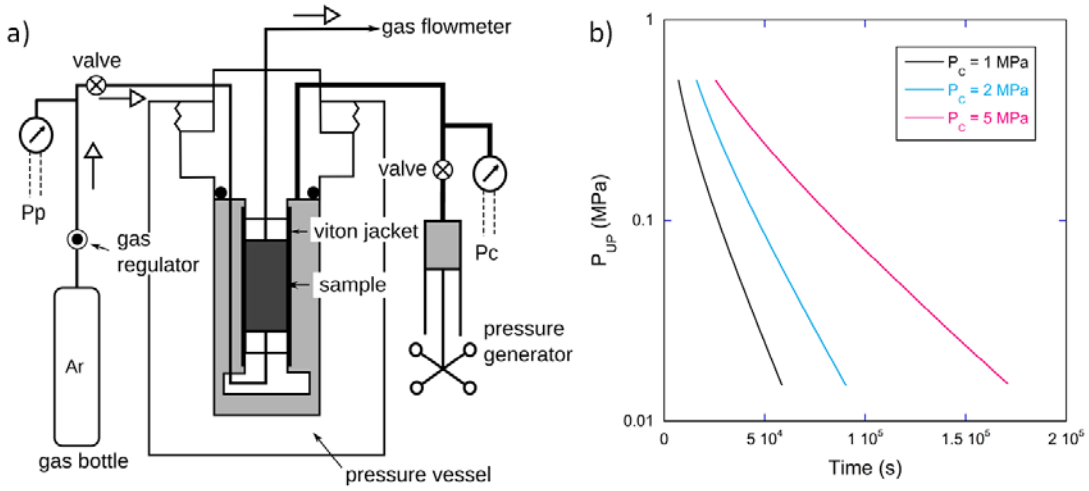

Figure 11. a) Experimental setup for measuring gas permeability in rock samples stressed up to 50 MPa hydrostatic confining pressure. b) Pressure decay curves on a semi-log plot obtained at confining pressures P_C of 1, 2 and 5 MPa respectively.

The time derivative of the pressure decay curve dP_{UP}/dt is calculated by applying a moving linear regression to the pressure decay curve over a constant number of points. The volume V_{UP} of the upstream gas circuit is either calibrated independently or by using the equation relating the outlet gas volume flow rate and the upstream pressure decay rate. At the upstream side of the sample, the inlet gas mass flow rate $Q^{M}_{UP}$is equal to:

$$Q^{M}_{UP} = \frac{M}{RT} V_{UP} \left| \frac{dP_{UP}}{dt} \right| \quad (4)$$

where M is the molar mass of the gas, R is the universal gas constant, and T is the temperature. Assuming that the gas mass stored in the sample can be neglected, we have $Q^{M}_{UP}=Q^{M}_{DOWN}$, where Q^{M}_{DOWN} is the outlet gas mass flow rate. The latter quantity can be expressed as a function of the measured outlet gas volume flow rate Q^{V}_{DOWN}:

$$Q^{M}_{DOWN} = \frac{M}{RT} P_{DOWN} Q^{V}_{DOWN} \quad (5)$$

Combining equations (4) and (5) yields a relationship between the outlet gas volume flow rate and the upstream gas pressure decrease rate that allows calculation of the upstream volume V_{UP}:

$$Q^{V}_{DOWN} = \frac{V_{UP}}{P_{DOWN}} \left| \frac{dP_{UP}}{dt} \right| \quad (6)$$

In Figure 12a, the linear relationship between outlet flow rate and inlet pressure time-derivative is shown for all three confining pressure levels. Assuming a constant atmospheric pressure P_{DOWN}, the volume of the upstream gas circuit is derived from the slope of this linear relationship following equation (6). Then the apparent gas permeability k_{gas} is estimated from equation (3) as a function of time and finally Klinkenberg's correction is applied to the data set in order to derive the true permeability k (see section 4.2). In Figure 12b, the gas permeability k_{gas} is plotted vs. inverse mean gas pressure $1/P_{MEAN}$ for the three tested confining pressures. As one can see, the linear trend is rather good, confirming that Klinkenberg's correction has to be applied. The true permeability k is then taken as the intercept of the best linear fit to each curve, and the Klinkenberg slip b factor is inferred from the slope. From the plot in Figure 12b the following results are obtained: at 5 MPa confining pressure (effective confining pressure between 4.5 and 5 MPa close to the KG²B pressure target) k=1.12 10^{-18} m² and b=0.33 MPa; at 2 MPa confining pressure k=2.26 10^{-18} m² and b=0.30 MPa; at 1 MPa confining pressure k=4.99 10^{-18} m² and b=0.15 MPa. The last point is to check the reproducibility, and hence the accuracy, of the measurements. This has been done by doubling each measurement at each confining pressure level. After the first measurement, the sample was allowed to rest at the prescribed confining pressure for one night, before repeating the above mentioned procedure. Repeatability is very good, with permeability variations lower than 2%.

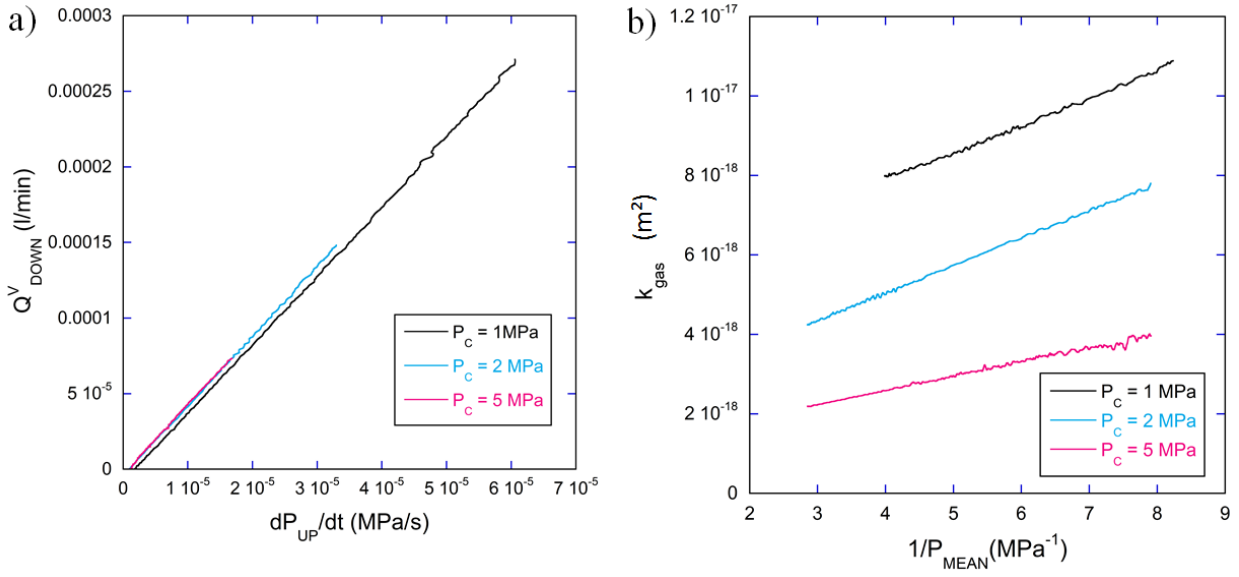

Figure 12. a) Linear relationship between outlet flow rate and inlet pressure decrease obtained at a confining pressure P_C of 1, 2 and 5 MPa respectively. b) Evolution of gas permeability k_{gas} with mean gas pressure for the three tested confining pressure levels.

The well-known and widely employed transient method based on the pulse decay technique described above has been extended recently (Lasseux and Jannot, 2011; Lasseux et al., 2012). The main purpose for the development of this new method is to avoid repeating several experiments at different values of P_{MEAN} to determine permeability k and slippage factor b. One could consider using an inverse technique applied to the complete unsteady flow model for the pulse-decay instead of the approximated analytical model of equation (1) so that these two parameters (along with porosity ϕ) could be identified on a single upstream pressure decay $P_{UP}(t)$ in the least square sense (Jannot et al., 2008). However, the sensitivity of the signal to these parameters were shown to be insufficient in the general case for a reliable identification (Lasseux et al., 2012). With the step-decay method, a downstream tank is introduced and both $P_{UP}(t)$ and $P_{DOWN}(t)$ are recorded, the former being taken as the input for the history matching that is carried out on the latter considered as the response. While $P_{UP}(t)$ can be modulated in any convenient way to improve sensitivity (a simple choice is a succession of steps, giving the name to the method of "step-decay"), it was shown that, for the interpretation: *i*) the volume of the upstream tank does not need to be known; *ii*) the presence of a dead volume between the upstream tank and the entrance of the porous sample, which represents a critical issue in the pulse decay method, is of no consequence on the measurement and can be ignored, *iii*) any irregularity on $P_{UP}(t)$, due to thermal effects or resulting from a leak at the upstream, will not introduce any bias in the interpretation as it is part of the input signal. Moreover, it was shown that, with this method, the three parameters, k, b and ϕ, can be simultaneously identified from a single experiment (Lasseux et al., 2012).

The step decay experiment was run with nitrogen at 30°C on a Grimsel granodiorite sub-core (length = 39.32 mm, diameter = 25.48 mm) that was first dried at 30°C for 3 weeks. The sample was placed in a Hassler sleeve and a confining pressure of 5.5 MPa was applied. The volume of V_{DOWN} was determined from 100 nitrogen pycnometry tests yielding V_{DOWN}=8.38 cm^3 with a standard deviation of 0.018 cm^3. Three different tests were carried out for which the applied average pore pressure difference over the different upstream pressure steps were 0.376 MPa (Test1, 4 steps), 0.275 MPa (Test2, 7 steps) and 0.327 MPa (Test3, 4 steps). The experimental recording times of $P_{UP}(t)$ and $P_{DOWN}(t)$ were 4h16min (Test1), 3h27min (Test2) and 1h10min (Test3).

The interpretation, using an inverse technique, is performed with a complete model with no assumption, except that the flow is isothermal and 1D in the x-direction within the sample which upstream and downstream faces are at x=0 and x=L, respectively while the gas is supposed to obey ideal gas law:

$$\frac{\partial^2 \Pi}{\partial x^2} = \frac{\phi\mu}{k}\frac{1}{\sqrt{\Pi}}\frac{\partial \Pi}{\partial t}, \quad \Pi = \Pi(x,t) = (P(x,t)+b)^2 \tag{7}$$

$$\Pi(x,0) = (P(x,0)+b)^2, \quad 0 \le x \le L \tag{8}$$

$$\Pi(0,t) = (P_{UP}(t)+b)^2, \quad t \ge 0 \tag{9}$$

$$\left.\frac{\partial \Pi}{\partial t}\right|_{x=L} = \frac{kA}{\mu V_{DOWN}}\left(\sqrt{\Pi}\frac{\partial \Pi}{\partial x}\right)_{x=L}, \quad t \ge 0 \tag{10}$$

The recorded evolution of $P_{UP}(t)$ and $P_{DOWN}(t)$ for Test1 are reported in Figure 13a. For the same experiment, the comparison between the measured signal $P_{DOWN}(t)$ and the signal

obtained at the end of the inverse procedure with the identified parameters k, b and ϕ in the least square sense is represented in Figure 13b, showing the excellent fit obtained with this procedure.

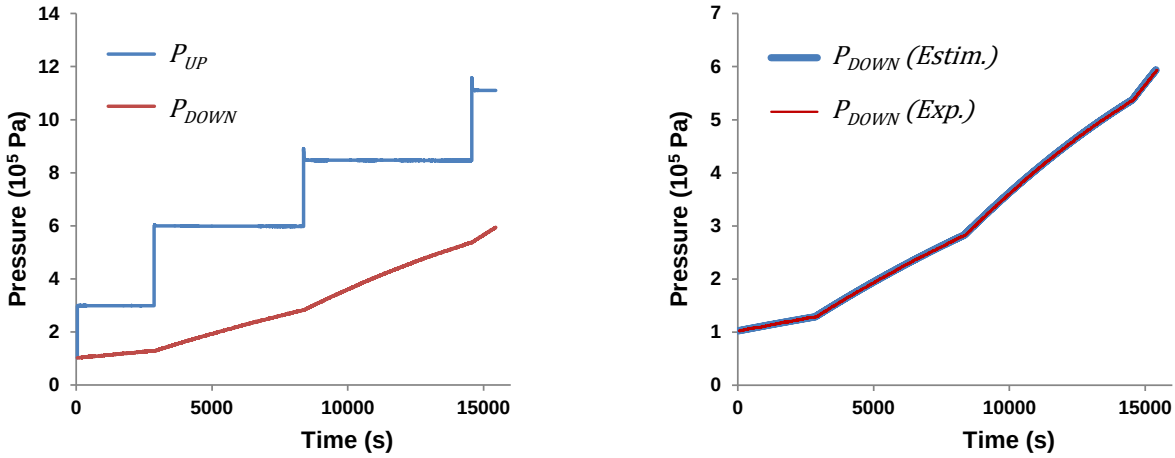

a) b)

Figure 13 a) Upstream ($P_{UP}(t)$) and downstream ($P_{DOWN}(t)$) pressure evolutions recorded during Test1. b) Downstream pressure signal measured during Test1 and obtained from the model with the fitted parameters k, b and ϕ at the end of the inverse procedure.

The fitted values of the parameters are respectively k=1.28 10^{-18} m², b=0.257 MPa and ϕ=0.012 for Test1; k=1.18 10^{-18} m², b=0.304 MPa and ϕ=0.008 for Test2; k=1.26 10^{-18} m², b=0.279 MPa and ϕ=0.012 for Test3. These values are consistent, in their trend, with the expected variations due to the difference between the confining pressure and the actual average pore pressure in the three different tests. Moreover, repeatability tests showed few percent of error on the above values.

3.6.3. Example of Oscillating Pore Pressure Method for Permeability Determination

[Contribution of Lab#18] Initially proposed by Turner (1958), the oscillation method was first applied to rocks by Kranz et al. (1990) and Fischer (1992). It uses a fixed-frequency, sinusoidally oscillating pore pressure signal applied at one end of the sample. The resultant (downstream) signal maintains the same period as the upstream signal, but is amplitude-attenuated and phase-shifted (Figure 14).

Bernabé et al. (2006) re-analyzed the oscillating pore pressure method and defined two independent dimensionless material parameters; η (dimensionless permeability) and ξ (dimensionless storativity ratio) which are functions of permeability (k, m²) and specimen storativity (β, Pa^{-1}) respectively and are defined:

$$\eta = \frac{A\tau k}{\pi L \mu \beta_D} \quad (11)$$

$$\xi = \frac{AL\beta}{\beta_D} \quad (12)$$

where A is the sample cross-sectional area (m²), τ is the oscillation period (s), L the sample length (m), β_D the downstream reservoir storage (m^3 Pa^{-1}) and μ the fluid viscosity (Pa s). Bernabé et al. (2006) improved upon the solutions presented by Kranz et al. (1990) and Fischer

(1992) by defining ξ and η such that each would be dependent on only one material parameter of the rock, thus allowing them to be assessed as independent material properties. In terms of ξ and η the solution to the diffusion equation is:

$$Ge^{-i\theta} = \left(\frac{1+i}{\sqrt{\xi\eta}}\sinh\left[(1+i)\sqrt{\frac{\xi}{\eta}}\right] + \cosh\left[(1+i)\sqrt{\frac{\xi}{\eta}}\right]\right)^{-1} \quad (13)$$

G is the ratio of downsteam to upstream wave amplitude (Gain) and θ is the phase shift between the upstream and downstream waveforms. Solving equation (13) to find G and θ using a range of valid values of η and ξ defines the region in which physically meaningful values of G and θ can be found. The region is limited by the lines ξ=0 and $\xi\rightarrow\infty$ (Bernabé et al., 2006). Sample storativity (β) is directly proportional to porosity (ϕ) and is given by:

$$\beta = \phi\left(C_f + C_p\right) \quad (14)$$

where C_f is the pore fluid compressibility and C_p is the compressibility of the porosity in response to changes in pore pressure at constant confining pressure. As $C_f \gg C_p$ the $C_f\,\phi$ term will dominate. Thus iso-ξ paths are nominally lines of constant porosity for a given value of downstream storage volume provided the compressibility of the pore fluid and the pores remain constant, there are no adsorption-desorption effects, and the sample behaves isotropically.

When the permeating fluid is a liquid its compressibility is small and varies only slowly with pressure, but for an ideal gas the compressibility is $1/P_p$, where P_p is the pore fluid pressure. At low temperatures T and high pressures gases become non ideal, expressed by the gas deviation factor Z in the gas law for a single mole:

$$P_p\,V = ZRT \quad (15)$$

where V is the gas volume and R is the universal gas constant. The gas compressibility is modified thus

$$c_f = \frac{1}{Pp} - \frac{1}{Z}\left(\frac{dZ}{dPp}\right)_T \quad (16)$$

For argon gas, for example, Gosman et al. (1969) show how Z varies with pressure, from which C_f (P_p) can be calculated. Viscosity of the pore fluid must also be known as a function of pressure and temperature. For liquids the viscosity varies only slowly with pressure and temperature, but larger variations apply for gases. Data for argon are provided in Michels et al. (1954) and Younglove and Hanley (1986).

Applying this method, it is usual to work with short core plugs, for example 25 mm in length and of similar diameter. Samples are jacketed in rubber tubing sealed to end pistons bearing a narrow (1mm diameter) hole to carry the pore fluid. Sintered metal discs are placed at each end of the specimen to diffuse the pore fluid across the whole diameter of the specimen. It is important that the jacket be pressed uniformly against the outer surface of the specimen to prevent short-circuit fluid paths. A steel blank can be used in lieu of a specimen to ensure that the experimental arrangements do not permit any unwanted fluid flow and for calibration of the

downstream volume. It is important to avoid any contamination of the specimen with liquid when gas is being used as a permeant. Liquid contamination will generally reduce apparent permeability.

The downstream volume (including pipework, downstream sintered plate and pressure transducer) must be determined as accurately as possible, and for very low permeability materials this volume will usually be as small as is feasible. Filler rods can be inserted into the pipes to minimize the volume further. For good resolution of low permeabilities a downstream volume of less than 500 mm^3 is desirable. The downstream pressure transducer must have high sensitivity (typically 0.02 MPa) and good stability.

A servo-controlled piston-cylinder pressure generator/volumometer is used to generate and control the pore pressure. This can be used to determine the downstream volume by first establishing an upstream pore pressure, then opening access to the downstream volume and measuring the volume of fluid that must be accepted to bring the downstream volume to the same pressure.

Experiments are typically carried out over a sequence of confining pressures at a fixed pore pressure in order to investigate the sensitivity of permeability to effective pressure. Initially it is important to raise the confining and pore pressures together such that the minimum desired effective pressure is not exceeded, to avoid permanent changes to permeability before permeability measurement at low effective pressure. The desired mean pore pressure and confining pressures are allowed to stabilize, with the open bypass valve linking upstream and downstream reservoirs. The bypass valve is closed slowly, to prevent buildup of unequal pore pressures and the upstream oscillation is started. The amplitude of the oscillation will typically be 1 MPa or less, to avoid violation of Darcy's law and pressure transients due to adiabatic heating and cooling. After any initial transient effects a downstream waveform at a constant mean pressure will develop, after which data from ~ 10 cycles will be collected (Figure 14).The period of the forcing waveform can be varied between about 60 seconds and several thousand seconds, in order to obtain a satisfactory gain ratio, ideally smaller than about 0.7.

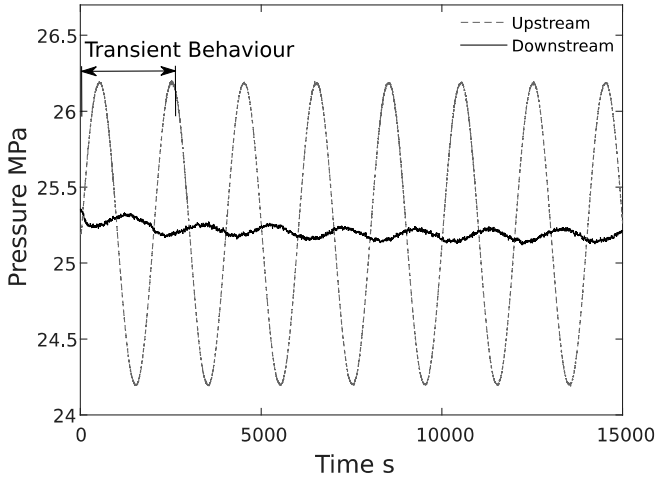

Figure 14. Example of oscillating pore pressure behaviour, showing amplitude attenuation of the forcing waveform and the phase shift of the downstream wave.

From these data the gain (ratio of downstream to upstream wave amplitudes) and phase shift must be determined. This can be done in several ways (i) from the Fourier transforms of the two waveforms (e.g. Faulkner and Rutter, 2000; Bernabé et al., 2006; Song et al., 2007), (ii) from the

parameters (orientation and axial ratio) of the Lissajou ellipses linking the two waveforms (e.g. Song et al., 2007) or (iii) by applying inverse amplitude ratio and phase shifts to match the two waveforms. The permeability is found by solving equation (13) iteratively for both η and ξ, from which permeability and storativity can be calculated. This can be done using a numerical equation solver. Initial values of ξ and η are obtained from a look-up table containing the values plotted in Figure 15a. The algorithm then seeks the values of ξ and η that simultaneously solve the modulus and argument of equation (13) that correspond to the measured amplitude ratio G and phase shift θ respectively.

Core plugs with three different orientations were taken from the main core section; the gneiss foliation plane is oriented 16° to the axis of the main core. Core A is parallel to the large core axis, Core B is normal to the main core axis and parallel to the foliation, and core C is perpendicular to the first two, nearly normal to the foliation. Helium pycnometry for four short core plugs yielded porosity 1.028±0.011%. Permeability for each core orientation was measured at a constant effective pressure (P_{eff}) of 4.5 MPa, at each of three different pore pressures, 5.5, 10.5 and 15.5 MPa (Figure 15b). Anisotropy is low, with the foliation-normal orientation displaying the lowest permeability (see section on anisotropy in the companion paper).

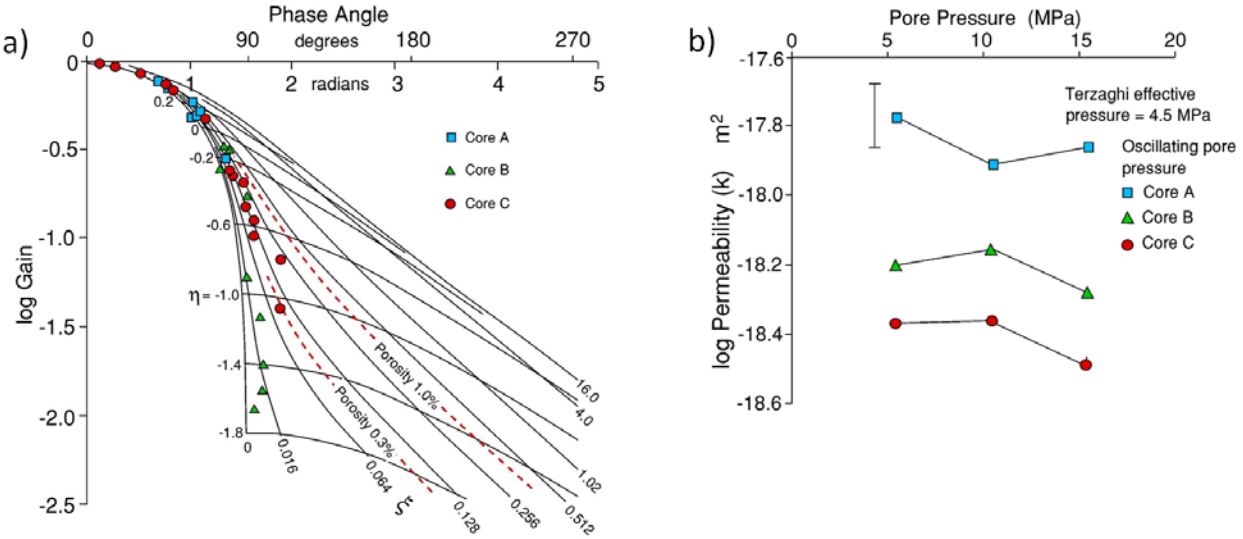

Figure 15. a) Solution space of equation (13) bounded by curves for ξ = 0 and 16, showing how gain and phase angle relate to η and ξ, with experimental results for KG²B cores A, B and C. b) Permeability vs. pore pressure at constant effective pressure (4.5 MPa) for the three cores.

The experimental data in Figure 15a plot well to the left of the expected trend for a porosity of 1.0%, and imply that flow does not access all pore space with equal facility. The sample storativity calculated using ξ from the oscillation technique is commonly found to be lower than the total storativity of the sample, calculated from porosity (ϕ), the known compressibility of the pore fluid using equation (12) (Fischer, 1992) and the downstream storage of the experimental setup. This is evident from the plot of log G versus phase shift θ for the Grimsel granodiorite (Figure 15a). The data lie along a track expected for a porosity of 0.3 % or smaller, compared with the track expected for the measured porosity. There is a weak indication that the deviation is greater for foliation-parallel flow than foliation-normal flow. Stronger

deviation is seen for anisotropically textured rocks (e.g. Mckernan et al., 2017), and suggests that for one-dimensional fluid flow a reduced fraction of the pore space is readily accessible. In contrast, porosity measurement when all faces of the specimen are equally accessible to permeating gas allows the full porosity to be measured.

4. Pressure Dependence of Permeability

The main target of the benchmarking exercise was permeability of the Grimsel granodiorite samples at 5 MPa effective pressure; in addition, on a voluntary basis, measurement at in situ effective pressure (30 MPa) was also encouraged. Several teams provided measurements at several pressures. Therefore we have: (i) single permeability values at 5 and 30 MPa (2-point analysis, 4 teams), (ii) multiple permeability values over an extended pressure range of 1 to 30 MPa (multi-point analysis, 9 teams). The complete data set is given in Table 1 and the results for the second data set are shown in Figure 16. Note that the effective pressure is defined here as the difference between confining and pore pressure, corresponding to an effective pressure coefficient equal to 1, in good agreement with the effective pressure law found by one participating lab (Figure 16a) showing that permeability measurements are nearly constant at fixed confining pressure minus pore pressure (2 MPa). It should also be noted that these data do not allow separation of pressure sensitivity in response to variations of effective pressure by varying total confining pressure at constant pore pressure, compared with varying pore pressure at a constant total confining pressure. Differences in behavior in this respect have been discussed for various rock types by several authors, (e.g. Heller et al., 2014; Kwon et al., 2001; Mckernan et al., 2017)

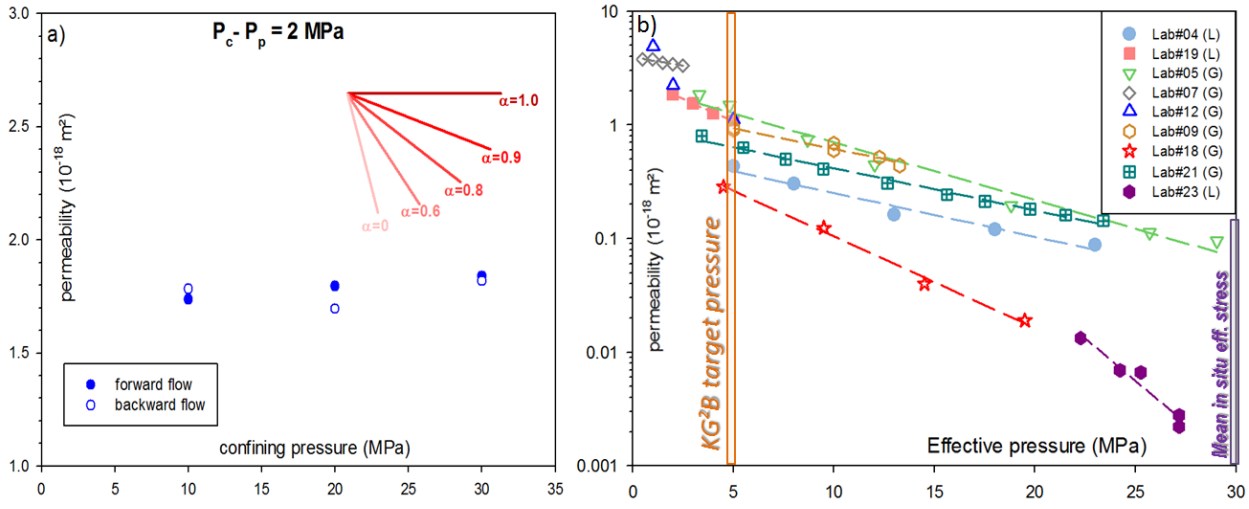

Figure 16. a) Test on effective pressure law by Lab#19 showing permeability measurements are consistent with α=1; b) Permeability vs. effective pressure. Solid symbols: measurements with liquid; open symbols: measurements with gas. All the measurements were made in the core axis direction.

A striking result is that the permeability evolution with effective pressure is generally linear on the semi-log plot: therefore the pressure-dependence of permeability can be accounted for using

an exponential law:

$$k = k_o \exp(-\gamma P_{eff}) \quad (17)$$

Such an exponential decrease is in agreement with the data compiled by David et al. (1994) for sedimentary and hard rocks. The stress-sensitivity parameter γ and zero-pressure permeability parameter k_o are given in Table 1.

	2-point analysis			multi-point analysis		
	perm (10^{-18} m²) @5MPa	**perm (10^{-18} m²) @30MPa**	**ratio**	**k_o (10^{-18} m²)**	**γ (MPa^{-1})**	**Comment**
Lab#02 (L)	**0.43**	**0.030**	14.3			
Lab#13 (L)	**0.91**	**0.277**	3.27			
Lab#14 (G)	**1.91**	**0.189**	10.1			
Lab#16 (G)	**1.81**	**0.155**	11.7			
Lab#04 (L)	**0.43**	*0.043*	10.0	0.609	0.0885	fit on 5 points
Lab#19 (L)	**1.08**	*0.0118*	91.4	2.65	0.180	fit on 4 points, low pressure range
Lab#23 (L)	*Not relevant*	*0.00101*	-	30.0	0.343	fit on 5 points, high pressure range
Lab#05 (G)	**1.46**	*0.068*	21.5	2.26	0.117	fit on 7 points
Lab#07 (G)	*2.78*	*0.474*	5.86	3.96	0.0707	fit on 5 points, low pressure range, axial stress only
Lab#12 (G)	**1.12**			not exponential		low pressure range
Lab#09 (G)	**0.92**	*0.115*	8.03	1.43	0.0842	fit on 6 points
Lab#18 (G)	**0.25**	*0.00257*	98.7	0.666	0.185	fit on 4 points, radial normal to foliation permeability
Lab#21 (G)	**0.83**	*0.0758*	10.9	0.975	0.0851	fit on 10 points

Table 1. Permeability measured at different effective pressures. For the multi-point analyses, exponential laws with parameters k_o and γ have been determined. Bold numbers are measurements; italic numbers are extrapolated values from the exponential law. All data were obtained for the axial core orientation unless otherwise stated.

In the pressure range above 5 MPa, four experiments (Lab#4, 5, 9 and 21) found quite consistent results, with an average stress-sensitivity parameter γ = 0.093+/-0.015 MPa^{-1} while two other

experiments found both lower permeability and stronger pressure dependence ($\gamma > 0.18$ MPa^{-1}), possibly because these samples might have lower crack density and with higher compliance and/or because of the different sample orientation (Lab#18) . In their compilation for crystalline, metamorphic and volcanic rocks, David et al. (1994) found that the stress-sensitivity parameter γ ranged between 0.023 and 0.11 MPa^{-1}; the Grimsel granodiorite is toward the higher end of this range. In the pressure range below 5 MPa, the pressure dependence seems also to be larger (except for Lab#07 who applied only axial stress). In this pressure range, one might both be impacted by crack closure and possibly leakage flow at the sample surface. From the 2-point analysis, we estimated the ratio $k(P_{eff}$ = 5 MPa) / $k(P_{eff}$ = 30 MPa) for both measured and extrapolated values (Table 1). Except two large values close to 100, most of the ratios range between 3.3 and 21 with an average value of 10.6. The Grimsel granodiorite exhibits a strong pressure dependence of permeability which can be well described by an exponential law.

5. Discussion

5.1. Outcome of the Benchmarking Exercise

Three main techniques were used to test sample permeability: steady-state flow that satisfies Darcy's law, pulse-decay (Brace et al., 1968) and oscillating flow (Fischer & Paterson, 1992; Kranz et al., 1990). The steady-state flow technique is often the simplest and easiest to interpret. Some rocks such as shales, clay-rich sandstones and fault gouge undergo time-dependent relaxation in response to pressure changes or the introduction of pore fluid. The steady-state method, which requires establishment of a constant flow rate, can be used to identify when transient changes in pore geometry have ended and a reliable measurement of permeability can be made. In some cases, the time needed for a sample to adjust to a new stress state can be in excess of a day (Morrow et al., 2014). If the sample has low permeability, then the flow rate due to an applied pressure gradient will be low, and water expelled as the sample compacts can result in erroneous flow rate determinations. Reversing the flow direction can help identify when time-dependent pore volume changes are important. Otherwise, it is best to confirm independently that changes in porosity have ceased before starting the flow test. For low permeability samples with small flow rates, both a high-accuracy flow sensor and a stable test chamber (especially controlled temperature) are needed for accurate determination of permeability (see Section 3.6.1). In describing flow in porous media, effects are separated between fluid properties (viscosity, μ) and pore geometry (permeability, k) with flow rate Q proportional to k/μ. Thus, for low permeability samples, increased flow rate can be accomplished by using a low-viscosity fluid, typically argon or nitrogen.

When testing low permeability crystalline rocks, accurate measurement of steady-state flow rate can be technically challenging. Brace et al. (1968) presented a transient pulse-decay technique that avoided this difficulty by measuring transient pressure changes rather than flow rate. This can be a fast and reliable method for measuring low permeability. It requires that the volume in closed chambers connected to the sample be optimized for the flow rate such that fluid flow through the sample produces a measurable pressure change over a convenient time interval. Similar to the steady-state technique, relaxation of pore volume in response to changes in stress state can produce pressure transients that mimic pressure transients from the pulse-decay test. Therefore, care must be taken to minimize these potential sources of error. On account of the small pressurized volumes used, the technique is very sensitive to any slow pressure leaks. Changes in ambient temperature can also lead to erroneous signals and need to be identified when making pulse-decay measurements.

The oscillating flow technique introduced for rocks in the early 1990's *(*Fischer, *1992;* Fischer & Paterson, 1992; Kranz et al., 1990) represents a significant advance in the measurement of flow properties of geologic materials. A time-independent oscillating pore pressure (generally a sine wave) is applied on one side of the sample and the amplitude and phase of the pressure in a chamber attached to the other side of the sample is recorded. The signal is time-stationary and can be stacked over multiple cycles to improve accuracy. In this case, both permeability and storativity (β) of the sample can be determined. There is a limited range in the frequency of the pressure oscillation and the volume of the downstream chamber over which accurate measurements can be made. In general, the downstream volume has to be larger than the pore volume in the test sample if storativity needs to be measured, but not so large as to affect adversely the sensitivity of the downstream pressure measurements.. Then, the period of the input signal that will produce a usable response will fall within a limited range that depends on the sample permeability. Measurement of lower permeability generally requires increased period of the sinusoid. If there is time-dependent relaxation of the sample, pressure on the downstream side will show a steady drift that often can be separated from the oscillating signal of known period. In the non-linear inversion procedure for analyzing the amplitude/phase data, k is not determined uniquely. Rather, the ratio k/β is determined and errors in k and β are correlated. Increasing the downstream reservoir solves this problem: permeability can then be estimated accurately but not storativity.

All reported determinations of permeability for the KG^2B core, measured at P_{eff} = 5 MPa in the axial direction, are plotted in Figure 17 along with standard deviation. Many uncertainties for individual measurements are smaller than the symbol size in the figure. Figure 5 shows that there is no indication that k varies systematically with distance from the tunnel (the same holds for porosity ϕ also, see companion paper). Pulse decay measurements are most abundant and tend to be higher than steady-state measurements. The two values that deviate the most from the mean value (both higher and lower) were steady-state measurements. Since measurements were carried out in different laboratories, using different samples and different techniques, the outlier values may be due to sample variability or test procedures. In the samples there is obvious foliation, anisotropy and sample variability on a scale comparable to the individual sample dimensions. A number of laboratories reported porosities of test samples spanning more than one order of magnitude (see companion paper) implying that much of the variability in permeability is the result of heterogeneity in the test samples.

Figures 3 and 4 show separate analyses of permeability determinations based on gas and liquid (primarily water) pore fluids. Average permeability determined using gas is about twice

the average permeability based on water measurements. This is consistent with Figure 17, where mean values and standard errors are plotted for different types of tests and different fluids. Permeability determinations are grouped by technique and working fluid. Some results plotted in Figure 17 are not statistically significant since three of the sub-categories only contain one or two measurements.

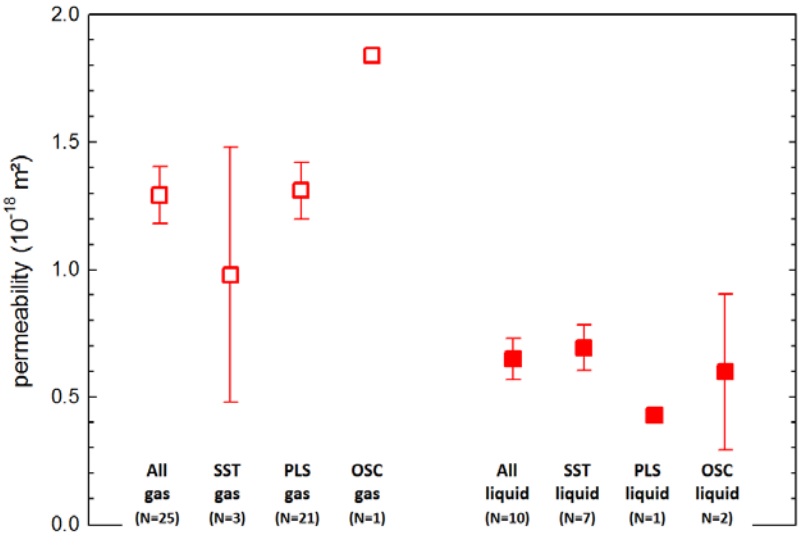

Figure 17. Summary of all the permeability results in the axial direction at 5 MPa effective pressure per fluid and method. The averaged measurements with gas are systematically larger than those with liquids.

Still, interesting trends can be seen. The left-most data point is the average permeability of all of the reported gas measurements (k = 1.29 10^{-18} m²). Average values for the three techniques using gas are adjacent. On the right side of the plot, the average permeability for all liquid measurements is plotted (k = 0.649 10^{-18} m²). Here the steady-state outlier values that were identified previously have been omitted. The correlation between permeability outliers and porosity values suggests that these samples were anomalous. Including them in the analysis has little effect on the mean value of permeability but increases uncertainty by about 3-fold. When the permeability values are separated into six sub-groups, there is no clear difference based on technique (steady-state, pulse decay or oscillating flow). However, a significant difference does exist in which gas permeability is about twice the permeability measured with liquid.

The choice of liquid or gas pore fluid can be problematic. For low permeability rocks and fault gouge, measurements can be completed much faster using gas, which has a relatively low viscosity. For some exceedingly tight samples, it may not be possible to obtain a usable flow rate with water as a pore fluid. At the same time, many samples have grain contacts and pore-filling minerals that are chemically reactive with water or brine. In this case, the choice of pore fluid becomes critical. Porosity filled with an inert gas may not have the same structure or pressure sensitivity as porosity filled with naturally occurring brine, or with water with which it is in chemical dis-equilibrium. This can cause water permeability to be up to 1-2 orders of magnitude lower than gas permeability. The reason for this phenomenon is not clear and various hypotheses are discussed in the literature, including core damage by clay plugging, clay swelling, structured water films on the mineral surfaces resulting in reduction of the effective transport volume, and electro-osmotic counter pressures (Faulkner & Rutter, 2000; Gray & Rex, 1966; Weber &

Stanjek, 2012). These issues may not be so important in crystalline rocks, but can be of major concern when measuring shales or clay-rich fault gouge.

Many of the permeability measurements had reported uncertainties of 1 to 2 percent. This appears to be a practical lower limit to the accuracy that can be obtained by any of the three techniques used. When all reported measurements are included and estimates are based on log(k), the standard error in estimating permeability is about 20%. The largest potential gain in reducing uncertainty appears to be related to the systematic difference between liquid and gas measurements. If this two-fold difference can be explained, the standard error might drop below 8%.

Two other important issues have been highlighted by the benchmarking exercise: the effect of sample size and the pressure sensitivity of permeability. Results were obtained on a large range of volumes, from 1 to 500 cm^3. Whereas the results for the largest samples were consistent, the permeability values for the smallest ones were scattered (Figure 6a) which may indicate that the volume of the smaller samples is below the REV. In this regard the choice of the Grimsel granodiorite, selected for its availability, convenience and relevance to geothermal energy studies, probably was not optimal. Foliation and mineralogical heterogeneity (Figure 6b) require to work on samples larger than the largest heterogeneity. Unfortunately this was not systematically the case. Despite the size effect, consistent results were found regarding pressure dependence, and showed that the Grimsel granodiorite is strongly pressure sensitive. The choice of a common effective confining pressure was a key for the success of the benchmarking exercise.

5.2 Offset between average gas and liquid permeability

Most of the permeability measurements were done using gas as the pore fluid (Figure 1), so it is important to assess the corrections for gas slippage. Intrinsic (or absolute) permeability is expected to be: i) determined only by the porous media structure, and ii) independent of the (homogeneous) working fluid passing through it. Nevertheless differences between water and gas permeability have been reported in literature for decades, and for several lithotypes (Muskat et al., 1937) including shales/mudrocks, tight sandstones and carbonates (e.g. Busch and Amann-Hildenbrand, 2013; Ghanizadeh et al., 2013; Amann-Hildenbrand et al., 2016). Klinkenberg (1941) introduced a theory regarding slip flow and its microscale effect: the slippage of gas molecules along capillary walls resulting in a non-zero wall velocity. He introduced a gas slippage parameter (or Klinkenberg slip factor) b relating the apparent gas permeability k_{app} to the mean (absolute) gas pressure P_{MEAN}:

$$k_{app} = k_{\infty}\left(1 + \frac{b}{P_{MEAN}}\right) \tag{18}$$

where k_{∞} is the permeability at infinite gas pressure (equivalent to the permeability k measured using a liquid). The slip of gas near a solid wall was first studied by Maxwell (1867) and Klinkenberg's concept of slippage was developed for gas flow within a bundle of constant radius capillaries. Hence, this theory may only be applicable within certain boundary conditions. Its

validity for flow in tortuous pore systems including bulges and bottlenecks or in crack-like porosity remains questionable.

Our study clearly shows differences depending on the fluid used. Gas permeability values appear to be about twice the permeability values obtained using liquids (Figure 4). This discrepancy is observed even after the Klinkenberg correction for gas slippage effects. Moreover the type of gas used is expected to have an effect as well. Gas permeability (both apparent and Klinkenberg corrected) has been observed to decrease in the order He > N_2 > CH_4 > CO_2, (e.g. Han et al., 2010). In organic rich material (coals, shales) this phenomenon is linked to sorption and swelling effects - in such cases a clear dependence upon total organic carbon can be identified. In the absence of sorption the fluid dynamic characteristics of the different gases have to be accounted for. Differences in molecule size and mean free path length result in different slip flow characteristics and, for larger gas molecules, in size exclusion.

The Klinkenberg slip factor values for each of the gas permeability experiments are plotted vs. the mean gas pressure in Figure 18a. Significant differences are observed between Helium, Argon, Nitrogen and air. The lowest slip factors *b* are found for air and Argon, followed by Helium. For Nitrogen, slip factor values span one order of magnitude, from 0.12 to 1.7 MPa, without noticeable dependence on mean pressure. Although several parameters can disturb the determination of slip factor *b* (accuracy of mean pressure value, lack of back pressure, inertia effects, effective pressure effects), it is surprising that such a large range of values was found for Nitrogen. Slip factor estimation is very sensitive to experimental procedures and several measurements along large mean pressure values are needed to ensure a robust regression in order to limit hazardous extrapolation for infinite mean pore pressure (McPhee and Arthur, 1991). In Figure 18b the *b* values are plotted vs. permeability. A weak linear trend is observed, in agreement with published results from tight sands, sandstones and shales (Jones & Owens, 1980; Amann-Hildenbrand et al., 2016; Fink et al., 2017). The three Argon data points are linked with a dashed line: these are measurements on a single sample at different confining pressures, showing a decreasing trend for *b* vs. permeability similar to published data on sedimentary rocks.

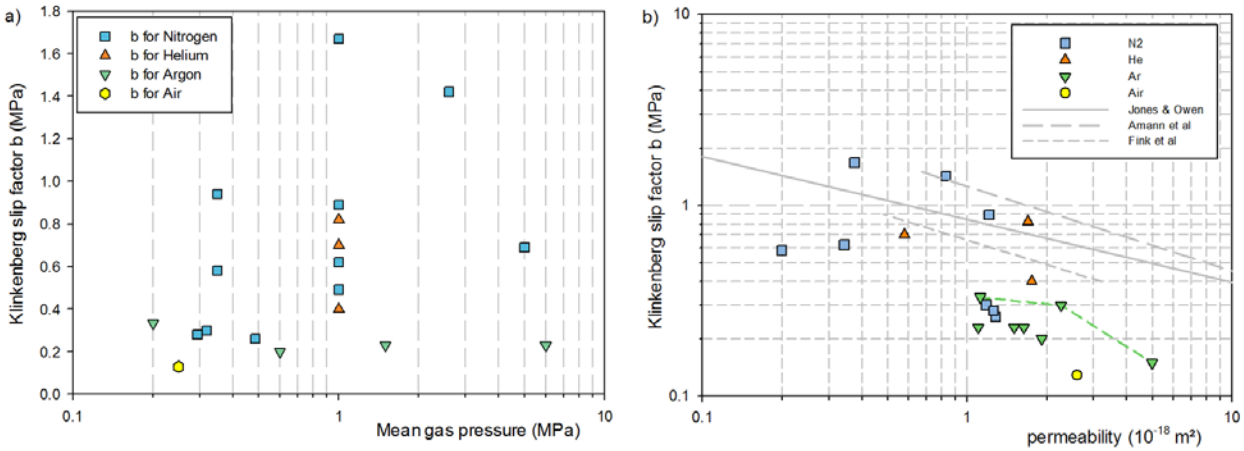

Figure 18. a) Klinkenberg slip factor *b* vs. mean pore pressure for gas permeability measurements with Klinkenberg correction. b) Klinkenberg slip factor *b* vs. permeability, grey lines are published data on gas sands (Jones & Owens, 1980), tight gas sandstones (Amann-Hildenbrand et al., 2016) and shale (Fink et al., 2017).

Flow in porous media is generally modeled under the assumption that the fluid is slow, continuous and viscous, with negligible flow of molecules adjacent to the pore wall (Darcy flow conditions). As mentioned above, the use of the Klinkenberg slip factor b is related to the hypothesis of a slippage flow regime at the microscale along capillary walls. The presence of high-surface-area minerals in the Grimsel granodiorite, such as biotite and chlorite, and their micro-pore structures, enhances diffusion, adsorption, and reactivity to gases and liquids. Specifically, if the gas or liquid exhibits chemical affinity with the biotite/chlorite minerals, then adsorption onto clay platelets, swelling and particle mobilization may occur. Under certain pressure and temperature conditions, the mean free path λ of the gas molecules (i.e. the average distance travelled without molecular collisions, depending on the temperature, the reciprocal mean pore pressure and the nature of the gas (McPhee & Arthur, 1991)) will exceed the size of pores/cracks. In such conditions, molecule/molecule collisions become so rare that the concept of viscosity becomes irrelevant, rendering the concept of continuum and bulk flow inapplicable. Knudsen number is classically used to quantify the validity or failure of the Navier-Stokes flow regime, defined as $K_n = \lambda/H$ where λ is the mean free path and H a characteristic hydrodynamic length scale (Hadjiconstantinou, 2006). For sake of simplicity, we take for H the crack aperture. When K_n is high, wall friction is reduced which can be interpreted as a decrease in viscosity leading to an apparent increase of permeability (Allan & Mavko, 2013; Carrigy et al., 2012). Depending on the magnitude of K_n, several flow regimes can be identified (Schaaf & Chambre, 1961; Wang et al., 2016). For example, when $0.01 < K_n < 0.1$ the flow is in the slippage flow regime and the Klinkenberg correction is applicable, but for $0.1 < K_n < 10$ the flow is in the transitional regime and the Klinkenberg correction may not be sufficient. In the latter case additional corrections need to be done to account for Knudsen diffusion flow. Following (Wang et al., 2016), the mean free path λ can be derived from a hard-sphere gas model and the Knudsen numbers are estimated using the following relation:

$$K_n = \frac{RT}{\pi\sqrt{2}(D_m)^2 r N_A P_{MEAN}} \tag{19}$$

where N_A is Avogadro's number, R the ideal gas constant, P_{MEAN} the average gas pressure, D_m the gas molecule diameter and T the absolute temperature of the gas. For the length scale H we take the average crack aperture obtained from microstructural analyses on the Grimsel granodiorite (H = 283 nm, see companion paper) and we allow this parameter to vary in the range 100 to 800 nm (see Figure 4A in the companion paper) . Knudsen numbers are plotted vs. the mean pore pressure in Figure 19 for all the gas permeability measurements.

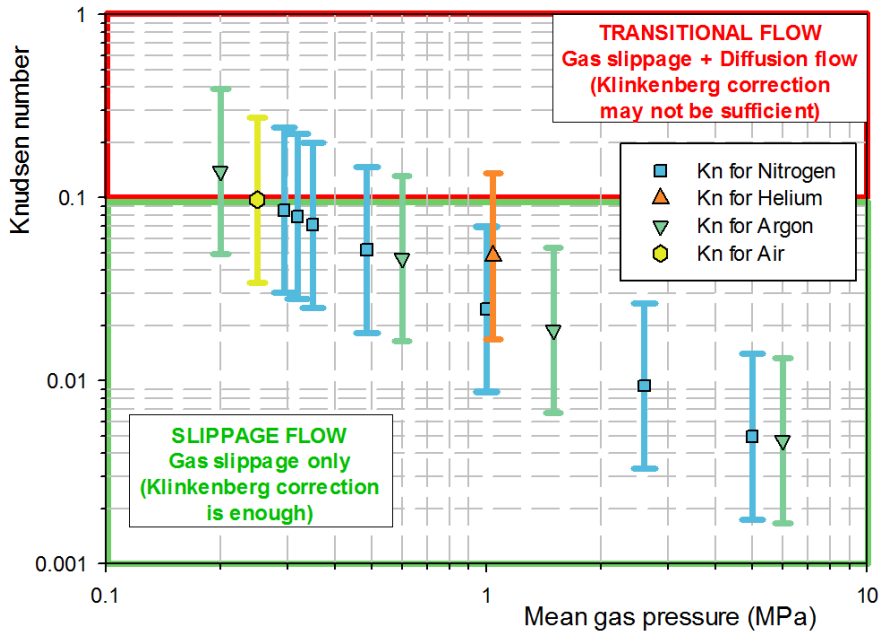

Figure 19. Knudsen numbers K_n vs. mean gas pressure for all the gas permeability experiments. The "error bars" correspond to a range of crack aperture from 100 to 800 nm, the symbols correspond to the average crack aperture (283 nm).

All the data points are located in the slippage flow region or close to the K_n=0.1 boundary. This suggests that the slippage flow has been correctly accounted for by the Klinkenberg correction. However complexity can arise from the pore size heterogeneity: in some pores the local Knudsen number may be very low while in others it may be high. Another assumption is that gases follow the ideal gas law, which might not always be true (e.g. in the event of water vapor contamination).

When gas transport in microporous rocks is dominated by gas diffusion through pores/cracks, the amount of gas adsorbed changes dynamically as pore pressure changes and is closely related to the properties of the adsorbate (viscosity and density) and solid adsorbent as well as the pore-space geometry (Cui et al., 2009; Silin and Kneafsey, 2012). In particular, since molecular collisions are controlled by the molecular kinetic energy, diffusion is controlled by pressure and temperature. Allan and Mavko (2013) show that a tortuous pore network with a static adsorbed layer experiences variable Knudsen diffusion as a function of pore pressure. Below a critical pore pressure, the effective permeability is significantly greater than the continuum prediction due to rarefaction of the gas and the onset of Knudsen diffusion. Above the critical pressure, the effect of Knudsen diffusion relative to adsorption is significantly reduced, resulting in effective permeability values up to 40% lower than the continuum prediction. It must also be noted that errors arise not only from measured values but also from computed ones.

Previous studies suggested that permeability tests should be performed using distilled water, because such water is expected to be inert. In fact, distilled water may cause sample leaching leading to the expansion of absorbed cations around clay particles and reducing hydraulic conductivity. Leaching can also mobilize particles due to either the expansion of diffuse double layers or the removal of cement (Wilkinson, 1969). This movement of particles results in 'dynamic permeability reduction' (Todd et al., 1978) caused by particle trapping at sub-critical pore throats. This dynamic permeability reduction can be regarded as non-reversible in the absence of dynamical stresses. Alternatives to distilled water include non-polar solvents, direct

use of field-collected water and duplication of the original pore water as permeant. Another common source of measurement error in very tight formations is entrapped gas, or air dissolved in the permeant while injecting it into the sample at high pressure. As pressure in the flowing water decreases, air can exsolve, causing pore clogging and erroneous measurements. Loosveldt et al. (2002) showed that water permeability was systematically lower than gas permeability, whereas ethanol permeability was intermediate. However, when gas permeability was corrected for the Klinkenberg effect, ethanol and gas permeabilities were found to be of the same order. In presence of chemical activity induced by polar fluids, Loosveldt et al. (2002) suggest that the Klinkenberg effect is only a small contributor to observed differences between gas and water permeability: other processes such as rehydration, dissolution/precipitation, migration of fine elements, and water adsorption in the smallest pores of the matrix may be more important.

Finally it may also be possible that liquids and gases do not probe the porous media in the same way: in such a situation, a common value of permeability is not expected at all between permeability measured with gases and liquids. Our data set suggests that in this case gases probe a more efficient pore network in terms of fluid transport than do liquids. Further studies are needed to support this viewpoint.

5.3. Source of Errors in Low Permeability Measurements

We discuss here the most common experimental problems and mechanisms for sources of error in permeability measurements from tight formations. The first source of error is methodological and procedural diversity that, to a large extent, controls the degree of variability in the results. The pressure pulse decay method is often the standard technique for low permeability material, as the conventional steady state method may not work if flow rate and/or differential pressure are too low to measure accurately. McPhee and Arthur (1991) showed that the effect of pressure transducer error (± 0.69 kPa) on the derived slip factor becomes more pronounced (~ 73%) when measurements are performed under constant flow rate mode (rather than constant differential pressure). When utilizing the pressure pulse decay method, extreme care must be taken to ensure constant temperature over the experiment so that the measured pressure changes are associated only with flow through the pore space. In addition, it may be difficult to reconcile gas or liquid permeabilities measured by laboratories that use different sleeve specifications and/or confining pressure. The extent to which the radial pressure on the sleeve is effectively transferred to the specimen is a function of sleeve hardness and thickness. If measurements refer to ambient conditions, sleeve confining pressure should be sufficiently high (1.5-5.5 MPa) for the sleeve to laterally seal the sample by filling its surface irregularities, thus avoiding fluid bypass, and sufficiently low to avoid permeability reduction due to pore volume compaction. This issue may become particularly relevant in the presence of schistose microstructure and large amounts of soft (compressible) minerals. When comparing data from different laboratories, it is important to decide *a priori* whether to emphasize the data from 'virgin' (unseasoned) samples during their first loading or limit the investigation to elastic regimes by pre-stressing the specimen.

The second source of error is associated with tight rock microstructure and solid-fluid interactions. The samples under investigation show visible foliation that relates to compositional banding (segregation of mineral phases). This mineralogical differentiation forms alternating layers of biotite and quartz (Schild et al., 2001), white mica and chlorite (Goncalves et al., 2012), and small amounts of chlorite/smectite (vermiculite), the latter resulting from alteration of biotite

layers (Kralik et al., 1992). The analyses conducted in this study show that a significant part of the pore space resides within the biotite phase as a network of sub-micron cracks exhibiting an average fracture aperture of 283 nm (see companion paper). Both mineralogical and microstructural features lead to processes that change the macro-scale permeability measured in the laboratory and its sensitivity to pressure.

5.4. Good Practice for Low Permeability Measurements

Experimental studies aim to determine of the “true” or “in-situ” permeability value andincrease understanding of contributing processes. However, the measured permeability depends on various parameters and their interdependencies. In the context of this study, reported permeability coefficients varied by approximately 1-2 orders of magnitude. Systematic and random errors are considered irrelevant here, as the experiments were performed at controlled temperature and pressure conditions, and any erratic fluctuations were accounted for in data analysis. The most important factors influencing the experimental results for single-phase flow were a) effective stress history and loading time, including stress-release effects due to coring, b) the pore fluid (gas, water) used in the experiments and c) sample heterogeneity. The latter category includes intrinsic lithological/textural features but also those induced by plug preparation, transportation and the drying/saturation procedure. The impact of each factor will differ among rock types, especially where swelling processes in clays can modify the pore space, in which case the choice of measuring fluid becomes a critical issue. In order to account for these different effects, the design and protocol of the experimental procedure, and data management must be discussed beforehand. In this benchmark study, laboratories were asked to submit their results in a standard form (see Figure 3 in David et al. (2017)), that contained all information required for thorough knowledge of the permeability estimation process (method, fluid, pressure and temperature conditions). However, in many cases it was extremely important to receive additional information including:

- Time information (absolute, relative) to identify whether the system had reached equilibrium with the applied pressure and temperature conditions and to investigate the effect of pressure cycling. The time required for pressure equilibration in low permeability material can be up to a month.

- In the case of gas permeability tests, additional data at all pressure steps should be provided: (i) apparent permeability and slip factor, (ii) mean pore pressure, (iii) pressure difference, (iv) absolute pressure, (v) temperature and equation of state for the gas. We recommend against averaging values obtained with different gases.

- Pressure history: the target effective pressure for a benchmarking exercise must never be exceeded during the loading stage prior to permeability measurement.

Based on this additional information, detailed study of transport processes becomes possible and any deviation from the expected behavior can be analyzed.

6. Conclusion

A benchmarking measurement exercise for low permeability material involving 24 laboratories allows us to discuss the influence of (i) pore-fluid, (ii) measurement method, (iii) sample size, (iv) pressure sensitivity and (v) gas slippage effects on the permeability of the selected rock, the Grimsel granodiorite. A complementary data set on (vi) microstructures and pore size distributions, (vii) porosity and (viii) permeability modeling is presented in a companion paper. In measurements at 5 MPa effective confining pressure, an average permeability of 1.47 10^{-18} m² was found, with a high standard deviation of 1.55 10^{-18} m² which can be explained by the presence of few outliers (4 of 39 values). Discarding those outliers yields an average permeability of 1.11 10^{-18} m² with a smaller standard deviation (0.57 10^{-18} m²). The most striking result was the large difference in average permeability between gas and liquid measurements: independently of the method used, gas permeability is higher than liquid permeability by approximately a factor 2 (k_{gas}=1.28 10^{-18} m² compared to k_{liquid}=0.65 10^{-18} m²). Possible explanations include (i) liquid permeability underestimated due to fluid-rock interactions (ii) gas permeability overestimated due to insufficient correction for gas slippage effects and/or (iii) gases and liquids do not probe exactly the same pore networks, and so there is no reason to expect a single permeability value. No decisive clue was found to favor one or the other explanation. However, the estimation of Knudsen numbers shows that all measurements using gas fell in the gas slippage regime and that no additional corrections are required to account for other gas flow. The larger scatter of permeability values for smaller samples seems to indicate that those samples have a volume below the REV, due to centimeter-sized mineralogical heterogeneities in the Grimsel granodiorite. Nevertheless our results are mostly self-consistent (except for few outliers) and in good agreement with other studies (Schild et al., 2001), especially the pressure dependence of permeability in the range 1 to 30 MPa. The permeability decrease with effective pressure can be described reasonably well with an exponential law, $k=k_o.\exp(-\gamma P_{eff})$ with γ=0.093 MPa^{-1}. Three examples of measurements are described in detail, using (i) the steady-state flow method, (ii) the transient pulse method and (iii) the pore pressure oscillation method: these experiments clearly show that many parameters need to be carefully controlled for successful permeability measurements in low permeability rocks. Another outcome of the benchmarking exercise was a set of good practice rules for measuring permeability in tight materials. A second round of benchmarking is currently under way with another tight material, the Cobourg Limestone. Additional challenges are expected in this benchmark (called KCL), as this rock has a permeability in the nano-Darcy range. With the experience gained with KG²B, the team is keen to take up this new challenge.

List of symbols

$\Delta P = P_{UP} - P_{DOWN}$, pore pressure difference (Pa)
μ, dynamic viscosity (Pa.s)
A, sample cross-sectional area (m²)
b, Klinkenberg slip factor (Pa)
BIB-SEM, broad ion beam – scanning electron microscopy

C_f, pore fluid compressibility (Pa^{-1})
C_p, pore compressibility in response to pore pressure changes (Pa^{-1})
D_m, gas molecule diameter (m)
FEBEX, Full-scale Engineered Barrier EXperiment
G, gain, downstream to upstream wave amplitude ratio
GTS, Grimsel Test Site
k, permeability (m^2)
k_∞, permeability at infinite gas pressure (m^2)
$k_{app}=k_{gas}$, apparent permeability measured with gas (m^2)
KG²B, K for Grimsel granodiorite benchmark
K_n, Knudsen number
k_o, permeability at zero effective pressure (m^2)
L, sample length (m)
MICP, mercury injection capillary pressure
N_A, Avogadro's number
P_∞, pressure at infinite time in pulse test (Pa)
P_{ATM}, atmospheric pressure (Pa)
P_c, confining pressure (Pa)
P_{DOWN}, downstream pore pressure (Pa)
$P_{eff} = P_c - P_p$, effective pressure (Pa)
P_{MEAN}, mean pore pressure (Pa)
P_p, pore pressure (Pa)
P_{UP}, upstream pore pressure (Pa)
$Q = Q^V = dV_P/dt$, volume flow rate (m^3/s)
$Q^M = dM/dt$, mass flow rate (kg/s)
R, universal gas constant ($J.mol^{-1}.K^{-1}$)
REV, representative elementary volume
rH, hydrodynamic length scale / crack aperture (m)
SAFOD, San Andreas Fault Observatory at Depth
T, absolute temperature (K)
t, time (s)
V, gas volume (m^3)
V_{DOWN}, downstream tubing volume (m^3)
V_P, pore volume (m^3)
V_{UP}, upstream tubing volume (m^3)
Z, gas deviation factor
ξ, dimensionless storativity ratio
α, decay factor in pulse test (s^{-1})
β, sample storativity (Pa^{-1})
β_D, downstream reservoir storage (m^3Pa^{-1})
ϕ, porosity
γ, permeability pressure dependence factor (Pa^{-1})
η, dimensionless permeability
λ, mean free path of a gas molecule (m)
θ, phase shift between upstream and downstream waveforms (rad)
τ, period of oscillation (s)

Acknowledgments and Data Availability Statement

This project was partially funded by a grant from the “Fondation de l’Université de Cergy-Pontoise”. We thank Belinda Godel for conducting the micro-CT study on a Grimsel granodiorite sample at CSIRO Perth. The KG^{2}B project is supported by the GIS Géosciences Franciliennes (http://www.geosciences-franciliennes.fr) within the research group on “Low Permeable Media”. We thank Yves Bernabé and Steve Ingebritsen for their thorough early review of both companion papers. All the data presented in this paper can be made available upon request.

References

Allan, A. M., and G. Mavko (2013), The effect of adsorption and Knudsen diffusion on the steady-state permeability of microporous rocks, *GEOPHYSICS*, *78*(2), D75–D83, doi:10.1190/geo2012-0334.1.

Alonso, E. E. et al. (2005), The FEBEX benchmark test: case definition and comparison of modeling approaches, *Int. J. Rock Mech. Min. Sci.*, *42*(5–6), 611–638, doi:10.1016/J.IJRMMS.2005.03.004.

Amann-Hildenbrand, A., J. P. Dietrichs, and B. M. Krooss (2016), Effective gas permeability of Tight Gas Sandstones as a function of capillary pressure - a non-steady-state approach, *Geofluids*, *16*(3), 367–383, doi:10.1111/gfl.12155.

Anez, L., S. Calas-Etienne, J. Primera, and T. Woignier (2014), Gas and liquid permeability in nano composites gels: Comparison of Knudsen and Klinkenberg correction factors, *Microporous Mesoporous Mater.*, *200*, 79–85, doi:10.1016/J.MICROMESO.2014.07.049.

Bernabé, Y., U. Mok, and B. Evans (2006), A note on the oscillating flow method for measuring rock permeability, *Int. J. Rock Mech. Min. Sci.*, *43*(2), 311–316, doi:10.1016/j.ijrmms.2005.04.013.

Blümling, P., F. Bernier, P. Lebon, and C. Derek Martin (2007), The excavation damaged zone in clay formations time-dependent behaviour and influence on performance assessment, *Phys. Chem. Earth, Parts A/B/C*, *32*(8–14), 588–599, doi:10.1016/J.PCE.2006.04.034.

Bossart, P., P. M. Meier, A. Moeri, T. Trick, and J.-C. Mayor (2002), Geological and hydraulic characterisation of the excavation disturbed zone in the Opalinus Clay of the Mont Terri Rock Laboratory, *Eng. Geol.*, *66*(1–2), 19–38, doi:10.1016/S0013-7952(01)00140-5.

Bourbie, T., and J. Walls (1982), Pulse Decay Permeability: Analytical Solution and Experimental Test, *Soc. Pet. Eng. J.*, *22*(5), 719–721, doi:10.2118/9744-PA.

Brace, W. F., J. B. Walsh, and W. T. Frangos (1968a), Permeability of granite under high pressure, *J. Geophys. Res.*, *73*(6), 2225–2236, doi:10.1029/JB073i006p02225.

Brace, W. F., J. B. Walsh, and W. T. Frangos (1968b), Permeability of granite under high pressure, *J. Geophys. Res.*, *73*(6), 2225–2236, doi:10.1029/JB073i006p02225.

Bruce, G. H., D. W. Peaceman, H. H. Rachford, and J. D. Rice (1953), Calculations of Unsteady-State Gas Flow Through Porous Media, *J. Pet. Technol.*, *5*(3), 79–92, doi:10.2118/221-G.

Busch, A., and A. Amann-Hildenbrand (2013), Predicting capillarity of mudrocks, *Mar. Pet. Geol.*, *45*, 208–223, doi:10.1016/j.marpetgeo.2013.05.005.

Carles, P., P. Eggermann, R. Lenormand, and J. M. Lombard (2007), Low permeability measurements using steady-state and transient methods, in *Symposium of the Society of Core Analysts*, Calgary.

Carrigy, N. B., L. M. Pant, S. Mitra, and M. Secanell (2012), Knudsen Diffusivity and Permeability of PEMFC Microporous Coated Gas Diffusion Layers for Different Polytetrafluoroethylene Loadings, *J. Electrochem. Soc.*, *160*(2), F81–F89, doi:10.1149/2.036302jes.

Cui, X., A. M. M. Bustin, and R. M. Bustin (2009), Measurements of gas permeability and diffusivity of tight reservoir rocks: Different approaches and their applications, *Geofluids*, *9*(3), 208–223, doi:10.1111/j.1468-8123.2009.00244.x.

Darcy, H. (1856), *Les Fontaines Publiques de la Ville de Dijon*, edited by E. Dalmont, Paris.

David, C., T.-F. Wong, W. Zhu, and J. Zhang (1994), Laboratory measurement of compaction-induced permeability change in porous rocks: Implications for the generation and maintenance of pore pressure excess in the crust, edited by C. J. Marone and M. L. Blanpied, *Pure Appl. Geophys. PAGEOPH*, *143*(1–3), 425–456, doi:10.1007/BF00874337.

David, C., J. Wassermann, and T. K. Team (2017a), The KG^2B project: a world-wide benchmark of low permeability measurement, in *Proceedings of the 6th Biot Conference on Poromechanics*, edited by S. G. M. Vandamme, P. Dangla, J.M. Pereira, pp. 1153–1161, Paris.

David, C., J. Wassermann, and The_KG^2B_Team (2017b), The KG^2B Project: A World-Wide Benchmark of Low Permeability Measurement, in *Poromechanics VI*, edited by M. Vandamme, P. Dangla, J. M. Pereira, and S. Ghabezloo, pp. 1153–1161, American Society of Civil Engineers, Reston, VA.

Faulkner, D. R., and E. H. Rutter (2000), Comparisons of water and argon permeability in natural clay-bearing fault gouge under high pressure at 20°C, *J. Geophys. Res. Solid Earth*, *105*(B7), 16415–16426, doi:10.1029/2000JB900134.

Fink, R., B. M. Krooss, and A. Amann-Hildenbrand (2017), Stress-dependence of porosity and permeability of the Upper Jurassic Bossier shale: an experimental study, *Geol. Soc. London, Spec. Publ.*, *454*(1), 107–130, doi:10.1144/SP454.2.

Fischer, G. J. (1992), The determination of permeability and storage capacity: Pore pressure oscillation method, in *Fault mechanics and transport properties of rocks : a festschrift in honor of W.F. Brace*, edited by B. (James B. Evans, T. Wong, and W. F. (William F. . Brace, pp. 187–211, Academic.

Fischer, G. J., and M. S. Paterson (1992), Measurement of Permeability and Storage Capacity in Rocks During Deformation at High Temperature and Pressure, pp. 213–252.

Fortin, J., S. Stanchits, S. Vinciguerra, and Y. Guéguen (2011), Influence of thermal and mechanical cracks on permeability and elastic wave velocities in a basalt from Mt. Etna volcano subjected to elevated pressure, *Tectonophysics*, *503*(1–2), 60–74, doi:10.1016/j.tecto.2010.09.028.

Ghanizadeh, A., M. Gasparik, A. Amann-Hildenbrand, Y. Gensterblum, and B. M. Krooss (2013), Lithological Controls on Matrix Permeability of Organic-rich Shales: An Experimental Study, *Energy Procedia*, *40*, 127–136, doi:10.1016/j.egypro.2013.08.016.

Goncalves, P., E. Oliot, D. Marquer, and J. A. D. Connoly (2012), Role of chemical processes on shear zone formation: an example from the Grimsel metagranodiorite (Aar massif, Central Alps), *J. Metamorph. Geol.*, *30*(7), 703–722, doi:10.1111/j.1525-1314.2012.00991.x.

Gray, D. H., and R. W. Rex (1966), Formation Damage in Sandstones caused by Clay Dispersion and Migration, *Clays Clay Miner.*, *14*, 355–366.

Hadjiconstantinou, N. G. (2006), The limits of Navier-Stokes theory and kinetic extensions for describing small-scale gaseous hydrodynamics, *Phys. Fluids*, *18*(11), 111301, doi:10.1063/1.2393436.

Han, F., A. Busch, B. M. Krooss, Z. Liu, N. van Wageningen, and J. Yang (2010), Experimental Study on Fluid Transport Processes in the Cleat and Matrix Systems of Coal, *Energy & Fuels*, *24*(12), 6653–6661, doi:10.1021/ef100165w.

Heller, R., J. Vermylen, and M. Zoback (2014), Experimental investigation of matrix permeability of gas shales, *Am. Assoc. Pet. Geol. Bull.*, *98*(5), 975–995, doi:10.1306/09231313023.

Hsieh, P. A., J. V. Tracy, C. E. Neuzil, J. D. Bredehoeft, and S. E. Silliman (1981), A transient laboratory method for determining the hydraulic properties of “tight” rocks—I. Theory, *Int. J. Rock Mech. Min. Sci. Geomech. Abstr.*, *18*(3), 245–252, doi:10.1016/0148-9062(81)90979-7.

Jakubick, A. T., and T. Franz (1993), Vacuum testing of the permeability of the excavation damaged zone, *Rock Mech. Rock Eng.*, *26*(2), 165–182, doi:10.1007/BF01023621.

Jannot, Y., D. Lasseux, G. Vizé, and G. Hamon (2007), A detailed analysis of permeability and Klinkenberg coefficient estimation from unsteady-state pulse-decay or draw-down experiments, in *Proc. Symp. Soc. Core Analysts*, p. 12 pp., Calgary.

Jannot, Y., D. Lasseux, L. Delottier, and G. Hamon (2008), A Simultaneous Determination of Permeability and Klinkenberg Coefficient From an Unsteady-State Pulse-Decay Experiment, in *Proc. Symp. Soc. Core Analysts*, p. 12 pp., Abu Dhabi.

Jones, F. O., and W. W. Owens (1980), A Laboratory Study of Low-Permeability Gas Sands, *J. Pet. Technol.*, *32*(9), 1631–1640, doi:10.2118/7551-PA.

Klinkenberg, L. J. (1941), The Permeability Of Porous Media To Liquids And Gases, *API Drill. Prod. Pr.*, 200–213.

Kralik, M., N. Clauer, R. Holnsteiner, H. Huemer, and F. Kappel (1992), Recurrent fault activity in the Grimsel Test Site (GTS, Switzerland): revealed by Rb-Sr, K-Ar and tritium isotope techniques, *J. Geol. Soc. London.*, *149*(2), 293–301, doi:10.1144/gsjgs.149.2.0293.

Kranz, R. L., J. S. Saltzman, and J. D. Blacic (1990a), Hydraulic diffusivity measurements on laboratory rock samples using an oscillating pore pressure method, *Int. J. Rock Mech. Min. Sci. Geomech. Abstr.*, *27*(5), 345–352, doi:10.1016/0148-9062(90)92709-N.

Kranz, R. L., J. S. Saltzman, and J. D. Blacic (1990b), Hydraulic diffusivity measurements on laboratory rock samples using an oscillating pore pressure method, *Int. J. Rock Mech. Min. Sci. Geomech. Abstr.*, *27*(5), 345–352, doi:10.1016/0148-9062(90)92709-N.

Kwon, O., A. K. Kronenberg, A. F. Gangi, and B. Johnson (2001), Permeability of Wilcox shale and its effective pressure law, *J. Geophys. Res. Solid Earth*, *106*(B9), 19339–19353, doi:10.1029/2001JB000273.

Lasseux, D., and Y. Jannot (2011), Measurement of parameters linked to the flow of fluids in a porous material,

Lasseux, D., Y. Jannot, S. Profice, M. Mallet, and G. Hamon (2012), The “Step Decay”: a new transient method for the simultaneous determination of intrinsic permeability, Klinkenberg coefficient and porosity on very tight rocks, in *Proc. Symp. Soc. Core Analysts*, p. 12 pp., Aberdeen.

Lenormand, R., F. Bauget, and G. Ringot (2010), Permeability measurement on small rock samples, in *Proc. Symp. Soc. Core Analysts*, p. 12 pp., Halifax.

Lieb, R. W. (1989), Presentation of the Grimsel Test Site, *Nucl. Eng. Des.*, *116*(1), 7–9, doi:10.1016/0029-5493(89)90198-2.

Lin, W. (1982), Parametric analyses of the transient method of measuring permeability, *J. Geophys. Res. Solid Earth*, *87*(B2), 1055–1060, doi:10.1029/JB087iB02p01055.

Lockner, D. ., C. Marone, and D. Saffer (2009), SAFOD Interlaboratory test, a progress report

(abstract), in *EatyhScope 2009 National Meeting*, Boise, ID, May 13-15.

Loosveldt, H., Z. Lafhaj, and F. Skoczylas (2002), Experimental study of gas and liquid permeability of a mortar, *Cem. Concr. Res.*, *32*(9), 1357–1363, doi:10.1016/S0008-8846(02)00793-7.

Makhnenko, R. Y., and J. F. Labuz (2013), Saturation of porous rock and measurement of the B coefficient, in *47th U.S. Rock Mechanics Symposium*, San Francisco.

Martin, J. C. (1959), Simplified Equations of Flow in Gas Drive Reservoirs and the Theorectical Foundation of Multiphase Pressure Buildup Analyses, *Trans. AIME*, *216*, 321–323, doi:10.2118/1235-G.

Maxwell, J. (1866), On the Dynamical Theory of Gases., *Proc. R. Soc. London*, *157*, 49–88.

Mckernan, R., J. Mecklenburgh, E. Rutter, and K. G. Taylor (2017), Microstructural controls on the pressure-dependent permeability of Whitby mudstone, in *Geomechanical and Petrophysical Properties of Mudrocks*, *Geological Society of London Special Publication*, edited by E. Rutter, J. Mecklenburgh, and K. Taylor, p. 454.

McPhee, C. A., and K. G. Arthur (1991), Klinkenberg Permeability Measurements: Problems and Practical Solutions, in *Advances in Core Evaluation II: Reservoir Appraisal*, pp. 371–392.

Michels, A., A. Botzen, and W. Schuurman (1954), The viscosity of argon at pressures up to 2000 atmospheres, *Physica*, *20*(7–12), 1141–1148, doi:10.1016/S0031-8914(54)80257-6.

Morrow, C. A., D. A. Lockner, D. E. Moore, and S. Hickman (2014), Deep permeability of the San Andreas Fault from San Andreas Fault Observatory at Depth (SAFOD) core samples, *J. Struct. Geol.*, *64*, 99–114, doi:10.1016/j.jsg.2013.09.009.

Muskat, M., and R. D. Wyckoff (1937), Flow of homogeneous fluids through porous media,

Neuzil, C. E., C. Cooley, S. E. Silliman, J. D. Bredehoeft, and P. A. Hsieh (1981), A transient laboratory method for determining the hydraulic properties of “tight” rocks—II. Application, *Int. J. Rock Mech. Min. Sci. Geomech. Abstr.*, *18*(3), 253–258, doi:10.1016/0148-9062(81)90980-3.

Ota, K., A. Möri, W. . Alexander, B. Frieg, and M. Schild (2003), Influence of the mode of matrix porosity determination on matrix diffusion calculations, *J. Contam. Hydrol.*, *61*(1), 131–145, doi:10.1016/S0169-7722(02)00139-0.

Pearson, F. J., C. Tournassat, and E. C. Gaucher (2011), Biogeochemical processes in a clay formation in situ experiment: Part E – Equilibrium controls on chemistry of pore water from the Opalinus Clay, Mont Terri Underground Research Laboratory, Switzerland, *Appl. Geochemistry*, *26*(6), 990–1008, doi:10.1016/J.APGEOCHEM.2011.03.008.

Rust, A. C., and K. V. Cashman (2004), Permeability of vesicular silicic magma: inertial and

hysteresis effects, *Earth Planet. Sci. Lett.*, *228*(1–2), 93–107, doi:10.1016/J.EPSL.2004.09.025.

Schaaf, S. A., and P. L. Chambre (1961), *Flow of Rarefied Gases*, Princeton University Press, Princeton.

Schild, M., S. Siegesmund, A. Vollbrecht, and M. Mazurek (2001), Characterization of granite matrix porosity and pore-space geometry by in situ and laboratory methods, *Geophys. J. Int.*, *146*(1), 111–125, doi:10.1046/j.0956-540X.2001.01427.x.

Selvadurai, A. P. S., M. J. Boulon, and T. S. Nguyen (2005), The Permeability of an Intact Granite, *Pure Appl. Geophys.*, *162*(2), 373–407, doi:10.1007/s00024-004-2606-2.

Silin, D., and T. J. Kneafsey (2012), Shale Gas: Nanometer-Scale Observations and Well Modeling, *J. Can. Pet. Technol.*, *51*(6), 464–475, doi:10.2118/149489-PA.

Song, I., and J. Renner (2007), Analysis of oscillatory fluid flow through rock samples, *Geophys. J. Int.*, *170*(1), 195–204, doi:10.1111/j.1365-246X.2007.03339.x.

Stewart, R. B., and R. T. Jacobsen (1989), Thermodynamic Properties of Argon from the Triple Point to 1200 K with Pressures to 100 MPa, *J. Phys. Chem. Ref. Data*, *18*(2), 639–798, doi:10.1063/1.555956.

Todd, A. C., J. Tweedie, and B. English (1978), Total Rock Characterisation Of North Sea Sandstones With Particular Reference To Interstitial Clays, in *SPE European Petroleum Conference*, Society of Petroleum Engineers.

Trimmer, D., B. Bonner, H. C. Heard, and A. Duba (1980), Effect of pressure and stress on water transport in intact and fractured gabbro and granite, *J. Geophys. Res.*, *85*(B12), 7059, doi:10.1029/JB085iB12p07059.

Turner, G. A. (1958), The flow-structure in packed beds, *Chem. Eng. Sci.*, *7*(3), 156–165, doi:10.1016/0009-2509(58)80022-6.

Wang, H. L., W. Y. Xu, M. Cai, and J. Zuo (2016), An Experimental Study on the Slippage Effect of Gas Flow in a Compact Rock, *Transp. Porous Media*, *112*(1), 117–137, doi:10.1007/s11242-016-0635-9.

Wassermann, J., J. C. Sabroux, S. Pontreau, S. Bondiguel, S. Guillon, P. Richon, and E. Pili (2011), Characterization and monitoring of the excavation damaged zone in fractured gneisses of the Roselend tunnel, French Alps, *Tectonophysics*, *503*(1–2), 155–164, doi:10.1016/J.TECTO.2010.10.013.

Weber, C., and H. Stanjek (2012), Development of diffuse double layers in column-wicking experiments: Implications for pH-dependent contact angles on quartz, *J. Colloid Interface Sci.*, *387*(1), 270–274, doi:10.1016/j.jcis.2012.07.074.

Wild, K., F. Amann, C. D. Martin, J. Wassermann, C. David, and M. Barla (2015a), Dilatancy of

clay shales and its impact on pore pressure evolution and effective stress for different triaxial stress paths, *49th US Rock Mech. / Geomech. Symp.*, (JUNE).

Wild, K. M., L. P. Wymann, S. Zimmer, R. Thoeny, and F. Amann (2015b), Water Retention Characteristics and State-Dependent Mechanical and Petro-Physical Properties of a Clay Shale, *Rock Mech. Rock Eng.*, *48*(2), 427–439, doi:10.1007/s00603-014-0565-1.

Wilkinson, W. B. (1969), In situ investigation in Soils and Rocks, *Br. Geotech. Soc. Inst. Civ. Eng. London*, 311–313.

Younglove, B. A., and H. J. M. Hanley (1986), The Viscosity and Thermal Conductivity Coefficients of Gaseous and Liquid Argon, *J. Phys. Chem. Ref. Data*, *15*(4), 1323–1337, doi:10.1063/1.555765.

Ziarani, A. S., and R. Aguilera (2012), Knudsen's Permeability Correction for Tight Porous Media, *Transp. Porous Media*, *91*(1), 239–260, doi:10.1007/s11242-011-9842-6.

Zinszner, B. (2007), A geoscientist's guide to petrophysics, *IFP Publ.*, xxi, 384 .

APPENDIX A

(3)The KG²B Team: the benchmark involved 24 rock physics laboratories around the world. In Figure A1 the logo of each participating institution is shown on a world map, with the benchmark logo and the collection of core samples sent to the participants. The name, e-mail addresses and institution of each participant and co-author are given in Table A1.

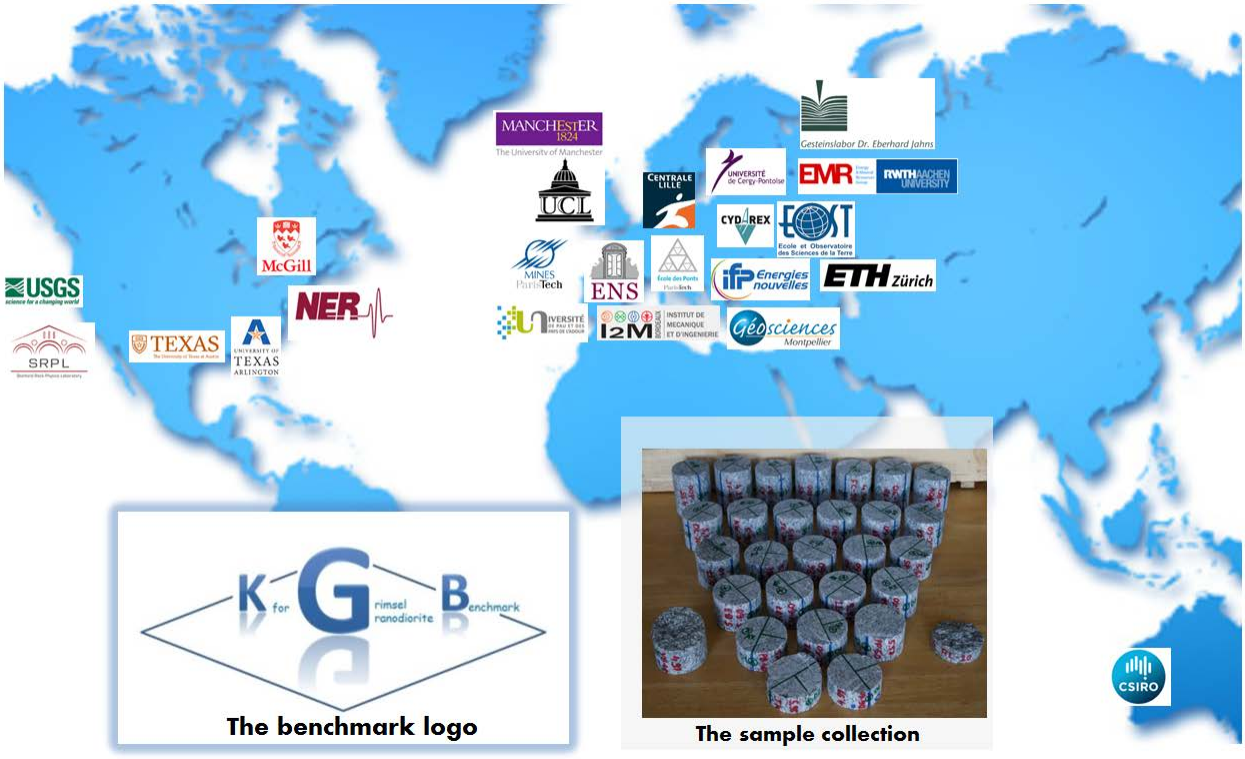

Figure A1. World map with the participants' logos, the benchmark logo and the core sample collection sent to the participants.

PARTICIPANTS (alphabetic order)	E-MAIL	INSTITUTION
Alexandra AMANN HILDENBRAND / Bernhard KROOSS	alexandra.amann@emr.rwth-aachen.de	EMR group, Aachen University, Germany
Guillaume BERTHE / Marc FLEURY	guillaume.berthe@ifpen.fr	IFPen, France
Joël BILLIOTTE	joel.billiotte@mines-paristech.fr	École des Mines de Paris, France
Christian DAVID / Jérôme WASSERMANN	christian.david@u-cergy.fr	Université Cergy-Pontoise, France
Catherine DAVY	catherine.davy@ec-lille.fr	Ecole Centrale de Lille, France
Pierre DELAGE / Philipp BRAUN	delage@cermes.enpc.fr	ENPC, France

Jérôme FORTIN	fortin@geologie.ens.fr	ENS Paris, France
David GRÉGOIRE / Laurent PERRIER	david.gregoire@univ-pau.fr	Université de Pau, France
Qinhong (Max) HU	maxhu@uta.edu	University of Texas, Arlington, USA
Eberhard JAHNS	jahns@gesteinslabor.de	Gesteinslabor, Germany
Jop KLAVER	jop.klaver@emr.rwth-aachen.de	Aachen University, Germany
Didier LASSEUX/Yves JANNOT/Alain SOMMIER	didier.lasseux@u-bordeaux.fr	I2M TREFLE, Bordeaux, France
Roland LENORMAND	roland.lenormand@cydarex.fr	Cydarex, France
David LOCKNER	dlockner@usgs.gov	USGS Menlo Park, USA
Laurent LOUIS / Gregory BOITNOTT	llouis@ner.com	New England Research, Vermont, USA
Claudio MADONNA / Florian AMANN	claudio.madonna@erdw.ethz.ch	ETH Zurich, Switzerland
Philip MEREDITH / John BROWNING / Tom MITCHELL	p.meredith@ucl.ac.uk	UCL Earth Sciences, UK
Franck NONO / Didier LOGGIA	nono@gm.univ-montp2.fr	Université Montpellier II, France
Peter POLITO	peter.Polito@jsg.utexas.edu	University of Texas, Austin, USA
Thierry REUSCHLÉ	thierry.reuschle@unistra.fr	EOST Strasbourg, France
Ernie RUTTER	ernie.rutter@manchester.ac.uk	Univ. Manchester, UK
Joël SAROUT / Lionel ESTEBAN	joel.sarout@csiro.au	CSIRO, Perth, Australia
Patrick SELVADURAI	patrick.selvadurai@mcgill.ca	McGill University, Canada
Tiziana VANORIO / Anthony CLARK	tvanorio@stanford.edu	Stanford University, USA

Table A1: The KG²B Team: list of participants and co-authors

APPENDIX B

Each participating laboratory was assigned a number following the core sample order, from #01 for the sample closest to the tunnel (at 4.17 m) to #24 for the deepest sample in the borehole (at 5.95 m). Table B1 provides sample location in the tunnel, the length and diameter of the sub-core drilled from the original core, and the method and pore fluid used for permeability measurements. Table B2 provides the permeability values measured at 5 MPa and (when available) at in situ stress 30 MPa. Note that porosity and radial permeability values have also been included in the table, although they are discussed in the companion paper.

	Distance from tunnel (m)	Sub-cored sample length (mm)	Sub-cored sample diameter (mm)	Method for permeability estimation	Fluid used for permeability measurement
Lab#01	4.17	25.6	25	Transient pulse & Step-decay (transient)	GAS (Argon)
	4.17	27.2	25		
	4.17	29.5	25		
Lab#02	4.25	83	40	Steady-state flow	LIQUID (water)
Lab#03	4.35	94	83 (no subcoring)	Steady-state flow	LIQUID (non degased water)
Lab#04	4.45	80	40	Transient pulse, Pore pressure oscillation & Modeling	LIQUID (brine)
Lab#05	4.63	25	38	Transient pulse & Modeling	GAS (Nitrogen)
Lab#06	4.78	86	hollow cylinder 83/60	Steady-state flow (radial flow)	LIQUID (distilled water)
Lab#07	4.94	1 to 5	chips	Transient pulse	GAS (Air)
Lab#08	4.99	21.4	19.5	Steady-state flow	GAS (Nitrogen)
		20.8	19.5		
Lab#09	5.04	50	40	Transient pulse	GAS (Nitrogen)
				Steady-state flow	LIQUID (deaerated tap water)
				Transient pulse	GAS (Argon)
Lab#10	5.11	31.5	29.9	Steady-state flow	LIQUID (water)
	5.11	28.3	30		
	5.11	28.8	30		
Lab#11	5.18	39.3	25.5	Step-decay (transient)	GAS (Nitrogen)
Lab#12	5.31	40	20	Transient pulse	GAS (Argon)
Lab#13	5.37	38	38	Steady-state flow	LIQUID (deionised water)
	5.37	20	20	Steady-state flow	
	5.37			Pore pressure oscillation	
Lab#14	5.42	41.3	64.6	Steady-state flow	GAS (Argon)

Lab#15	5.47	15	15 (cube)	Microstructure analysis (MICP) & Modeling	*NA*
Lab#16	5.52	44	38	Complex transient technique	GAS (Nitrogen)
	5.52	42	38		
Lab#17	5.57	21.5	25.4	Transient pulse	GAS (Argon)
Lab#18	5.67	30	26	Pore pressure oscillation & Transient pulse	GAS (Argon)
	5.67	30	26		
	5.67	30	26		
Lab#19	5.72	33.6	83.3 (no subcoring)	Steady-state flow	LIQUID (deionized water)
Lab#20	5.77	49.9	25.4	Transient pulse	GAS (Helium and Nitrogen)
	5.77	49.3	25.3		
	5.77	35.6	25.4		
Lab#21	5.83	38.9	39	Steady-state flow	GAS (Nitrogen)
Lab#22	5.9	39	25.4	Transient pulse	GAS (Argon)
		38	25.4		
		38.9	25.4		
Lab#23	5.95	24.2	38.3	Steady-state flow	LIQUID (degassed tap water)
				Steady-state flow & Transient pulse	GAS (Helium and Nitrogen)
Lab#24	5.95	thin section	thin section	Microstructure analysis (BIB-SEM) & Modeling	*NA*

Table B1: List of samples with distance to the borehole mouth, length and diameter, and methods used for permeability estimation with corresponding fluids.

LAB#	**Fluid**	**Method**	**Porosity (%)**	**Axial PERM@5_MPa (10^{-18} m²)**	**Axial PERM@30_MPa (10^{-18} m²)**	**Radial PERM@5_MPa (10^{-18} m²)**
#01	Gas	PLS		1.1		
	Gas	PLS		1.5		
	Gas	PLS		1.63		
#02	Liquid	SST		0.43	0.03	
#03	Liquid	SST	0.6	0.6	0.04	
#04	Liquid	PLS	0.62	0.43	0.055 (*)	
#04	Liquid	OSC	0.62	0.294		
#05	Gas	PLS	0.6	1.46	0.064 (*)	

#06		SST				0.84 @1.75MPa
#07	Gas	PLS	0.7	2.6 (*)		
#08	Gas	SST				0.243
	Gas	SST		0.199		
#09	Gas	PLS	0.8	1.3		
	Liquid	SST	0.8	0.94		
	Gas	PLS	0.8	1.49		
	Gas	PLS	0.8	1.37		
#10	Liquid	SST	0.46	0.5		
	Liquid	SST	0.17	0.05 (**)		
	Liquid	SST	0.51	0.73		
#11	Gas	PLS	1.16	1.28		
	Gas	PLS	0.78	1.18		
	Gas	PLS	1.18	1.26		
#12	Gas	PLS	0.52	1.12		
#13	Liquid	SST		8.35 (**)	2.06 (**)	
	Liquid	SST		4.73 (**)		
	Liquid	SST		0.579		
	Liquid	OSC		0.906	0.277	
#14	Gas	SST	0.73	1.91	0.189	
#16	Gas	PLS	0.23	1.69		
	Gas	PLS	0.43	1.81	0.155	
#17		PLS	1.8			0.66
#18	Gas	OSC	1.03	1.84		
	Gas	OSC	1.03			0.843
	Gas	OSC	1.03			0.501
#19	Liquid	SST		1.08		
#20	Gas	PLS	0.51	0.579		
	Gas	PLS	0.51	0.342		
	Gas	PLS	0.88	1.69		
	Gas	PLS	0.88	0.375		
	Gas	PLS	1.29	1.75		

	Gas	PLS	1.29	1.21		
#21	Gas	SST	1.5	0.83	0.07 (*)	
#22	Gas	PLS	0.7	0.795		
	Gas	PLS	0.5			0.825
#23	Liquid	SST	0.26	5.4 (**)		

Table B2: Permeability and porosity values. (*) extrapolated values; (**) outliers discarded from the global analysis (SST=Steady-state flow method, PLS=Transient pulse method, OSC=Oscillating pore pressure method).

1494